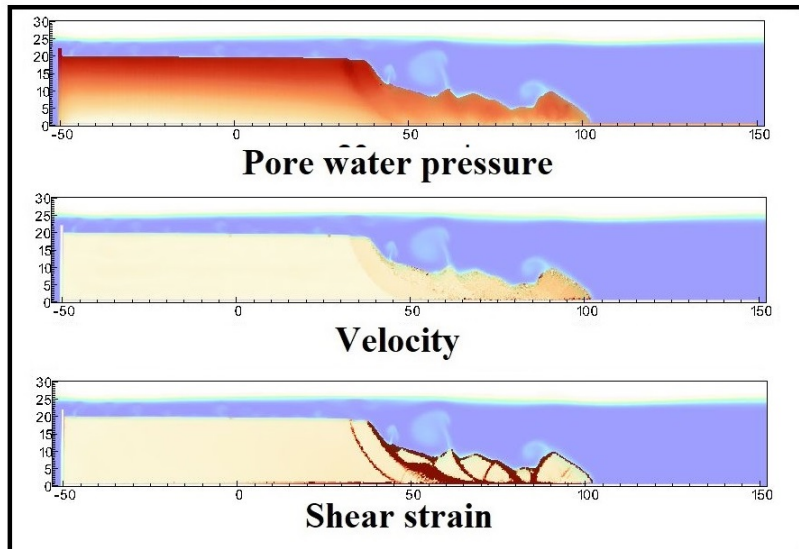


- 1 Graphical Abstract
- 2 MPMICE: A hybrid MPM-CFD model for simulating coupled problems in porous media. Application to earthquake-induced submarine landslides
- 3 Quoc Anh Tran, Gustav Grimstad, Seyed Ali Ghoreishian Amiri



Application to earthquake-induced submarine landslide

₆ Highlights

₇ **MPMICE: A hybrid MPM-CFD model for simulating coupled prob-**
₈ **lems in porous media. Application to earthquake-induced subma-**
₉ **rine landslides**

₁₀ Quoc Anh Tran, Gustav Grimstad, Seyed Ali Ghoreishian Amiri

- ₁₁ • MPMICE is introduced for multiphase flow in porous media.
- ₁₂ • Material Point method allows to model large deformation of non-isothermal
₁₃ porous media.
- ₁₄ • ICE (compressible multi-material CFD formulation) allows ~~to stabilize~~
₁₅ stabilizing pore water pressure and turbulent flow.
- ₁₆ • MPMICE is validated and apply to simulate the earthquake-induced
₁₇ submarine landslide.

¹⁸ MPMICE: A hybrid MPM-CFD model for simulating
¹⁹ coupled problems in porous media. Application to
²⁰ earthquake-induced submarine landslides

²¹ Quoc Anh Tran^a, Gustav Grimstad^a, Seyed Ali Ghoreishian Amiri^a

^a*Norwegian University of Science and Technology, , Trondheim, 7034, Norway*

²² Abstract

²³ In this paper, we describe a soil-fluid-structure interaction model that com-
²⁴ bines soil mechanics (saturated sediments), fluid mechanics (seawater or air),
²⁵ and solid mechanics (structures). The formulation combines the Material
²⁶ Point Method, which models large deformation of the porous media and the
²⁷ structure, with the Implicit Continuous-fluid Eulerian, which models com-
²⁸ plex fluid flows. We validate the model and simulate the whole process of
²⁹ earthquake-induced submarine landslides. We show that this model captures
³⁰ complex interactions between saturated sediment, seawater, and structure,
³¹ so we can use the model to estimate the impact of potential submarine land-
³² slides on offshore structures.

³³ *Keywords:*

³⁴ Material Point Method, MPMICE, submarine landslide.

35	Contents	
36	Nomenclature	4
37	Introduction	6
38	Theory and formulation	8
39	Assumptions	8
40	Governing equations	9
41	Constitutive soil model	11
42	Turbulent model	12
43	Frictional force for soil-structure interaction	12
44	Momentum and Energy exchange model	13
45	Solving momentum and energy exchange with an implicit solver	15
46	Equation of state for fluid phases	16
47	Numerical implementation	17
48	Interpolation from Solid Particle to Grid	18
49	Compute equation of state for fluid phase	20
50	Compute face-centered velocity Compute cell face velocity	21
51	Compute face-centered temperature Compute cell face temperature	22
52	Compute fluid pressure (implicit scheme)	22
53	Compute viscous shear stress term of the fluid phase	23
54	Compute nodal internal temperature of the solid phase	23
55	Compute and integrate acceleration of the solid phase	23
56	Compute Lagrangian value (mass, momentum and energy)	24
57	Compute Lagrangian specific volume of the fluid phase	25
58	Compute advection term and advance in time	26
59	Interpolate from cell to node of the solid phase	27
60	Update the particle variables	27
61	Numerical examples	28
62	Fluid Flow through isothermal porous media	28
63	Isothermal consolidation	29
64	Thermal induced cavity flow	30
65	Underwater debris flow	32
66	Validation of soil response to the seismic loading	35
67	Earthquake-induced submarine landslides	39

68	Conclusions	44
69	Acknowledgements	45
70	Appendix: Equation derivation	45
71	Evolution of porosity	46
72	Momentum conservation	46
73	Energy conservation	47
74	Advanced Fluid Pressure	48
75	Momentum and Energy exchange with an implicit solver	49

⁷⁶ **Nomenclature**

General variables

<u>Variable</u>	<u>Dimensions</u>	<u>Description</u>
V	$[L^3]$	Representative volume
n		Porosity
σ	$[ML^{-1}t^{-2}]$	Total stress tensor
Δt	$[t]$	Time increment
\mathbf{b}	$[ML^1t^{-2}]$	Body force
c_v	$[L^2t^{-2}T^{-1}]$	Constant volume specific heat
f_d	$[MLt^{-2}]$	Drag forces in momentum exchange term
f^{int}	$[MLt^{-2}]$	Internal forces
f^{ext}	$[MLt^{-2}]$	External forces
q_{fs}	$[MLt^{-2}]$	Heat exchange term
S		Weighting function
∇S		Gradient of weighting function

⁷⁷

Solid phase

<u>Variable</u>	<u>Dimensions</u>	<u>Description</u>
m_s	$[M]$	Solid mass
ρ_s	$[ML^{-3}]$	Solid density
ϕ_s		Solid volume fraction
$\bar{\rho}_s$	$[ML^{-3}]$	Bulk Solid density
\mathbf{x}_s	$[L]$	Solid Position vector
\mathbf{U}_s	$[Lt^{-1}]$	Solid Velocity vector
\mathbf{a}_s	$[Lt^{-2}]$	Solid Acceleration vector
σ'	$[ML^{-1}t^{-2}]$	Effective Stress tensor
ϵ_s		Strain tensor
e_s	$[L^2t^{-2}]$	Solid Internal energy per unit mass
T_s	$[T]$	Solid Temperature
\mathbf{F}_s		Solid Deformation gradient
V_s	$[L^3]$	Solid Volume

Fluid phase

<u>Variable</u>	<u>Dimensions</u>	<u>Description</u>
m_f	[M]	Fluid mass
ρ_f	[ML ⁻³]	Fluid density
ϕ_f		Fluid volume fraction
$\bar{\rho}_f$	[ML ⁻³]	Bulk Fluid density
\mathbf{U}_f	[Lt ⁻¹]	Fluid Velocity vector
$\boldsymbol{\sigma}_f$	[ML ⁻¹ t ⁻²]	Fluid stress tensor
p_f	[ML ⁻¹ t ⁻²]	Fluid isotropic pressure
$\boldsymbol{\tau}_f$	[ML ⁻¹ t ⁻²]	Fluid shear stress tensor
e_f	[L ² t ⁻²]	Fluid Internal energy per unit mass
T_f	[T]	Fluid Temperature
v_f	[L ³ /M]	Fluid Specific volume $\frac{1}{\rho_f}$
α_f	[1/T]	Thermal expansion
μ	[ML ⁻¹ t ⁻¹]	Fluid viscosity
V_f	[L ³]	Fluid Volume

Superscript

<u>Variable</u>	<u>Dimensions</u>	<u>Description</u>
n		Current time step
L		Lagrangian values
$n + 1$		Next time step

Subscript

c	Cell-centered quantity
p	Particle quantity
i	Node quantity
FC	Face-centered Cell face quantity
L, R	Left and Right cell faces

79 **Introduction**

80 Many geological natural processes and their interactions with man-made
81 structures are influenced by soil-fluid-structure interactions. The prediction
82 of these processes requires a tool that can capture complex interactions
83 between soil, fluid, and structure, such as the process of submarine land-
84 slides. Indeed, The offshore infrastructure as well as coastal communities
85 may be vulnerable to submarine landslides. Submarine landslides contain
86 three stages: triggering, failure, and post-failure. Erosion or earthquakes can
87 trigger slope failures in the first stage. Following the failure, sediments move
88 quickly after the post-failure stage. In other words, solid-like sediments will
89 behave like a fluid after failure. This phase transition makes the simulation
90 of submarine landslides a challenging task.

91

92 Due to this phase transition, submarine landslide can be modeled by ei-
93 ther the Computational Fluid Dynamics (CFD) or the particle-based meth-
94 ods. For simulating submarine slides, CFD methods solve governing equa-
95 tions in a full-Eulerian framework [1, 2, 3, 4] with interface capturing tech-
96 niques. While CFD can handle complex flows (such as turbulent flows), it
97 cannot account for the triggering mechanism of submarine landslides because
98 it is not ~~straightforward~~ straightforward to consider 'soil constitutive laws' of
99 sediment materials in the Eulerian framework. In contrast, particle-based
100 methods can overcome this problem by using the Lagrangian framework.
101 These methods have been extensively used to simulate landslides, like Mate-
102 rial Point Method (MPM) [5], Smooth Particle Hydro Dynamics [6], Particle
103 Finite Element Method [7], or Coupled Eulerian Lagrangian Method [8]. For
104 simplicity, these simulations adopt total stress analysis which neglects the
105 pore pressure development which is key factor triggering slope failures.

106

107 Recent developments in particle-based methods model the coupling of
108 fluid flows in porous media by sets of Lagrangian particles. For the MPM
109 family, it is the double-point MPM ([9, 10, 11]) where fluid particles and
110 solid particles are overlapped in a single computational grid. Even if fluid
111 flows are considered, particle-based methods have numerical instability in
112 modeling the fluid flow, which requires additional numerical treatments such
113 as the B-bar method [9], null-space filter [12], or least square approximation
114 [13, 14]. Indeed, CFD is a more optimal option for complex fluid flows
115 especially dealing with large distortions of continuum fluid media. Therefore,

116 it could be ideal to combine the CFD with particle-based methods. More than
 117 50 particle-based methods have been developed to solve large deformations
 118 of solids over the last two decades [15], but the MPM appears to be the
 119 best candidate for coupling with the CFD. Because MPM incorporates a
 120 stationary mesh during computation, just like CFD. As such, both MPM
 121 and CFD can be coupled naturally in a unified computational mesh.



Figure 1: Interaction between soil-fluid-structure

122

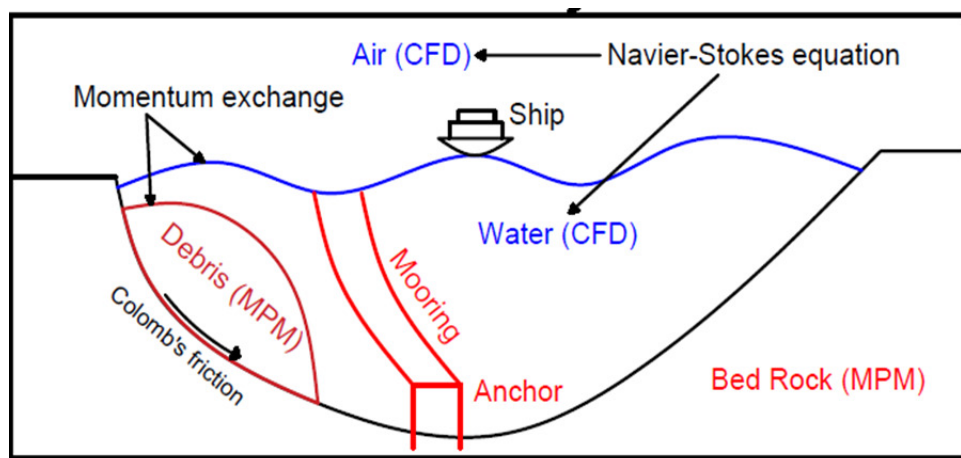


Figure 2: Coupling of soil-water-structure interaction using MPMICE

123 A numerical method for simulating soil-fluid-structure interaction (Figure
124 1) involving large deformations, is presented in this work in order to simu-
125 late the interaction between sediment (soil), seawater (fluid) and offshore
126 structures (structure) namely MPMICE (Figure 2). In the MPMICE, the
127 Material Point Method (MPM) is coupled with the Implicit Continuous Eu-
128 lerian (ICE). The MPM method is a particle method that allows the porous
129 soil to undergo arbitrary distortions. The ICE method, on the other hand,
130 is a conservative finite volume technique with all state variables located at
131 the cell center (temperature, velocity, mass, pressure). An initial technical
132 report [16] at Los Alamos National Laboratory provided the theoretical and
133 algorithmic foundation for the MPMICE, followed by the MPMICE devel-
134 opment and implementation in the high-performance Uintah computational
135 framework for simulating fluid-structure interactions [17]. This paper pri-
136 marily contributes ~~further~~ further to the development of the MPMICE for
137 analyzing the **soil**-fluid-structure interaction, since sediment should be con-
138 sidered as a porous media (soil) and not as a solid to capture the evolution
139 of the pore water pressure. Baumgarten et al. [18] made the first attempt
140 at coupling the Finite Volume Method with the MPM for the simulation of
141 soil-fluid interaction. In contrast to the mentioned work, we use implicit time
142 integration for the multi phase flows instead of explicit time integration for
143 the single-phase flow.

144 **Theory and formulation**

145 This section lay out the theoretical framework for the MPMICE model.
146 We use the common notation of the continuum ~~meehaniees~~ mechanics with
147 vector and tensor denoted simply by using bold font and scalar denoted by
148 using normal font. The notation are shown in Nomenclature.

149 *Assumptions*

150 The following assumptions are made for the MPMICE model.

- 151 1. Solid phases (MPM) are described in a Lagrangian formulation while
152 fluid phases (ICE) are described in an Eulerian formulation in the
153 framework of continuum mechanics and mixture theory.
- 154 2. Solid grains are incompressible while the fluid phases are compressible.
155 Solid's thermal expansion is negligible.
- 156 3. There is no mass exchange between solid and fluid phases.
- 157 4. Terzaghi's effective stress is valid.

158 *Governing equations*

159 A representative element volume Ω is decomposed by two domains: solid
160 domains Ω_s and fluid domains Ω_f . Then, all domains are homogenized
161 into two overlapping continua. Considering the volume fraction of solid
162 $\phi_s = \Omega_s/\Omega$ and fluid $\phi_f = \Omega_f/\Omega$ with the true (or Eulerian) porosity
163 $n = \sum \phi_f$ of the representative element volume, the average density of solid
164 and fluid phases are defined as:

165

$$\bar{\rho}_s = \phi_s \rho_s, \quad \bar{\rho}_f = \phi_f \rho_f \quad (1)$$

166 The mass of solid and fluid phases are:

167

$$m_s = \int_{\Omega_s} \rho_s dV = \bar{\rho}_s V, \quad m_f = \int_{\Omega_f} \rho_f dV = \bar{\rho}_f V \quad (2)$$

168 Reviewing the Terzaghi's effective stress concept for the saturated porous
169 media, the total stress σ is calculated by:

170

$$\sigma = \sigma' - p_f I \quad (3)$$

171 The balance equations are derived based on the mixture theory. The rep-
172 resentative thermodynamic state of the fluid phases are given by the vector
173 $[m_f, \mathbf{U}_f, e_f, T_f, v_f]$ which are mass, velocity, internal energy, temperature,
174 specific volume. The representative state of the solid phases are given by the
175 vector $[m_s, \mathbf{U}_s, e_s, T_s, \sigma', p_f]$ which are mass, velocity, internal energy, temper-
176 ature, effective stress and pore water pressure. The derivation is presented
177 in detail in the Appendix.

178

179 **Mass Conservation**

180 The mass balance equations for both fluid (e.g., water, air) and solid phases
181 are:

182

$$\frac{1}{V} \frac{\partial m_f}{\partial t} + \nabla \cdot (m_f \mathbf{U}_f) = 0, \quad \frac{1}{V} \frac{D_s m_s}{Dt} = 0 \quad (4)$$

183 Solving the mass balance equation [of the solid phase](#) leads to:

$$\frac{D_s n}{Dt} = \phi_s \nabla \cdot \mathbf{U}_s \quad (5)$$

184

185 **Momentum Conservation**

¹⁸⁶ The momentum balance ~~equation-equations~~ for the fluid phases (e.g., water,
¹⁸⁷ air) are:

$$\frac{1}{V} \left[\frac{\partial(m_f \mathbf{U}_f)}{\partial t} + \nabla \cdot (m_f \mathbf{U}_f \mathbf{U}_f) \right] = -\phi_f \nabla p_f + \nabla \cdot \boldsymbol{\tau}_f + \bar{\rho}_f \mathbf{b} + \sum \mathbf{f}_d \quad (6)$$

¹⁸⁸ The momentum balance ~~equation-equations~~ for the solid phases are:

$$\frac{1}{V} \frac{D_s(m_s \mathbf{U}_s)}{Dt} = \nabla \cdot (\boldsymbol{\sigma}') - \phi_s \nabla p_f + \bar{\rho}_s \mathbf{b} + \sum \mathbf{f}_{fric} - \sum \mathbf{f}_d \quad (7)$$

¹⁸⁹

¹⁹⁰ Energy Conservation

¹⁹¹ The internal energy balance ~~equation-equations~~ for the fluid phases (e.g.,
¹⁹² water, air) are:

$$\frac{1}{V} \left[\frac{\partial(m_f e_f)}{\partial t} + \nabla \cdot (m_f e_f \mathbf{U}_f) \right] = -\bar{\rho}_f p_f \frac{D_f v_f}{Dt} + \boldsymbol{\tau}_f : \nabla \mathbf{U}_f + \nabla \cdot \mathbf{q}_f + \sum q_{sf} \quad (8)$$

¹⁹³ The internal energy balance ~~equation-equations~~ for the solid phase ~~is~~are:

$$\frac{m_s}{V} c_v \frac{D_s(T_s)}{Dt} = \boldsymbol{\sigma}' : \frac{D_s(\boldsymbol{\epsilon}_s^p)}{Dt} + \nabla \cdot \mathbf{q}_s - \sum q_{sf} \quad (9)$$

¹⁹⁴ where c_v is the specific heat at constant volume of the solid materials.
¹⁹⁵

¹⁹⁶ Closing the systems of equations, the following additional models are needed:

¹⁹⁷ (1) A constitutive equation to describe the stress - strain behaviour of solid
¹⁹⁸ phase (computing effective stress $\boldsymbol{\sigma}'$).

¹⁹⁹ (2) Optional turbulent model to compute the viscous shear stress $\boldsymbol{\tau}_f$.

²⁰⁰ (3) Frictional forces \mathbf{f}_{fric} for the contact for soil-structure interaction be-
²⁰¹ tween solid/porous materials with the friction coefficient μ_{fric} .

²⁰² (4) Exchange momentum models (computing drag force \mathbf{f}_d) for interaction
²⁰³ between materials.

²⁰⁴ (5) Energy exchange models (computing temerature exhange term q_{sf}) for
²⁰⁵ interaction between materials.

²⁰⁶ (6) An equation of state to establish relations between thermodynamics vari-
²⁰⁷ ables of each fluid materials $[P_f, \bar{\rho}_f, v_f, T_f, e_f]$.

²⁰⁸ Four thermodynamic relations for the equation of states are:

$$\begin{aligned} e_f &= e_f(T_f, v_f) \\ P_f &= P_f(T_f, v_f) \\ \phi_f &= v_f \bar{\rho}_f \\ 0 &= n - \sum_{f=1}^{N_f} v_f \bar{\rho}_f \end{aligned} \quad (10)$$

²⁰⁹ *Constitutive soil model*

²¹⁰ As a result of the explicit MPM formulation, we can derive the constitutive law in the updated Lagrangian framework of "small strain - large deformation". Therefore, the rotation of the particles (representative element volume) is manipulated by rotating the Cauchy stress tensor. First, ²¹⁴ the deformation gradient is decomposed into the polar rotation tensor \mathbf{R}_s^{n+1} and sketch-stretch ²¹⁵ tensor \mathbf{V}_s^{n+1} as:

$$\mathbf{F}_s^{n+1} = \mathbf{V}_s^{n+1} \mathbf{R}_s^{n+1} \quad (11)$$

²¹⁶ Then, before calling the constitutive model, the stress and strain rate tensor ²¹⁷ are rotated to the reference configuration as:

$$\boldsymbol{\sigma}'^{n*} = (\mathbf{R}_s^{n+1})^T \boldsymbol{\sigma}'^{\textcolor{red}{n*}} \mathbf{R}_s^{n+1} \quad (12)$$

$$\delta\boldsymbol{\epsilon}^{n*} = (\mathbf{R}_s^{n+1})^T \delta\boldsymbol{\epsilon}_{\textcolor{red}{s}}^{\textcolor{blue}{n*}} \mathbf{R}_s^{n+1} \quad (13)$$

²¹⁹ Using the constitutive model with the input tensors $\boldsymbol{\sigma}'^{n*}, \delta\boldsymbol{\epsilon}^{n*}$ to compute ²²⁰ the Cauchy stress tensor at the advanced time step $\boldsymbol{\sigma}'^{n+1*}$ then rotating it ²²¹ back to current configuration as:

$$\boldsymbol{\sigma}'^{n+1} = \mathbf{R}_s^{n+1} \boldsymbol{\sigma}'^{n+1*} (\mathbf{R}_s^{n+1})^T \quad (14)$$

²²² In this paper, we adopt the hyper-elastic Neo Hookean model for the structure ²²³ materials and additionally Mohr-Coulomb failure criteria for the soil (porous ²²⁴ media) materials. The Cauchy stress of the hyper-elastic Neo Hookean model ²²⁵ can be written as:

$$\boldsymbol{\sigma}' = \frac{\lambda \ln(J)}{J} + \frac{\mu}{J} (\mathbf{F}\mathbf{F}^T - \mathbf{J}) \quad (15)$$

226 where λ and μ are bulk and shear modulus ad J is the determinant of the
 227 deformation gradient \mathbf{F} . And the yield function f and flow potentials g of
 228 the Mohr-Coulomb can be written as:

$$f = \frac{\sigma'_1 - \sigma'_3 - 2c + 2c' \cos(\phi')}{\sigma'_1 + \sigma'_3} \sin(\phi') \quad (16)$$

$$g = \frac{\sigma'_1 - \sigma'_3 - 2c + 2c' \cos(\psi')}{\sigma'_1 + \sigma'_3} \sin(\psi')$$

229 where the In the equations, c' , ϕ' , and ψ' are cohesion and friction angle represent
 230 the cohesion, friction angle, and dilation angle, respectively. σ'_1 and σ'_3
 231 are denote the maximum and minimum principal stress stresses, with the
 232 condition $\sigma'_1 < \sigma'_3 < 0$. It is important to note that in our assumptions,
 233 stress is considered positive during extension, which means the signs of the
 234 stresses in these equations are opposite to those in standard Soil Mechanic's
 235 textbooks.

236 Turbulent model

237 The turbulent effect is modelled using a statistical approach namely large-
 238 eddy simulation. In this approach, the micro-scale turbulent influence in the
 239 dynamics of the macro-scale motion is computed through simple models like
 240 Smagorinsky model. In the Smagorinsky mode model, the residual stress
 241 tensor is:

$$\tau_{ij} = 2\mu_{eff}(\bar{S}_{ij} - \frac{1}{3}\delta_{ij}\bar{S}_{kk}) + \frac{1}{3}\delta_{ij}\tau_{kk} \quad (17)$$

242 where the strain rate tensor is given by:

$$\bar{S}_{ij} = \frac{1}{2}(\frac{\delta \bar{U}_i}{\delta x_j} + \frac{\delta \bar{U}_j}{\delta x_i}) \quad (18)$$

243 and the effective viscosity is sum of molecular viscosity and turbulent vis-
 244 cosity $\mu_{eff} = \mu + \mu_t$ in which the turbulent viscosity μ_t is calculated by:

$$\mu_t = (C_s \Delta)^2 \sqrt{2\bar{S}_{ij}\bar{S}_{ij}} \quad (19)$$

246 where C_s is the Smagorinsky constant with the value of 0.1 and $\Delta = \sqrt[3]{dxdydz}$
 247 is the grid size that defines the subgrid length scale.

248 Frictional force for soil-structure interaction

249 MPMICE includes a contact law for the interaction between
 250 soil and structure using the first Coulomb friction contact for MPM presented

251 by Bardenhagen et al. ([19]). The magnitude of the friction force at the
 252 contact depends on the friction coefficient μ_{fric} and the normal force \mathbf{f}_{norm}
 253 computed from the projection of the contact force in the normal direction.

$$\mathbf{f}_{fric} = \mu_{fric} \mathbf{f}_{norm} \quad (20)$$

254 The contact determines whether the soil is sliding or sticking to the structure
 255 by comparing the friction force with the sticking force \mathbf{f}_{stick} computed from
 256 the projection of the contact force in the tangent direction as:

$$\begin{aligned} & \text{if } \mathbf{f}_{fric} \geq \mathbf{f}_{stick} \text{ no sliding} \\ & \text{if } \mathbf{f}_{fric} < \mathbf{f}_{stick} \text{ sliding occurs} \end{aligned} \quad (21)$$

257 Frictional sliding between solid materials also generates dissipation and the
 258 work rate generated from the sliding can be calculated as:

$$\Delta W_{friction} = \mathbf{f}_{fric} d \quad (22)$$

259 where d is the sliding distance which can be computed based on the sliding
 260 velocity between two materials.

261 *Momentum and Energy exchange model*

262 Currently, the energy exchange coefficient H_{sf} is assumed to be constant
 263 for the sake of simplicity. Then the energy exchange can be written as:

$$q_{sf} = H_{sf}(T_f - T_s) \quad (23)$$

264 On the other hand, the drag force can be calculated as:

$$f_d = K(\mathbf{U}_s - \mathbf{U}_f) \quad (24)$$

265 For the momentum exchange between fluid flows and porous media, we as-
 266 sume that the drag force \mathbf{f}_d depends on the average grain size of the grains D_p ,
 267 the porosity n , the fluid ~~vieosity~~viscosity μ_f , and is ~~propotional~~proportional
 268 to the relative velocities of soil grains and fluid $(\mathbf{U}_s - \mathbf{U}_f)$. Based on recent
 269 investigation of CFD simulations of fluid flow around mono- and bi-disperse
 270 packing of spheres for $0.1 < \phi_s < 0.6$ and $Re < 1000$ [20]. The drag force is
 271 given by:

272

$$\mathbf{f}_d = \frac{18\phi_s(1-\phi_s)\mu_f}{D_p^2} F(\phi_s, Re)(\mathbf{U}_s - \mathbf{U}_f) \quad (25)$$

²⁷³ where Reynolds number Re are computed as:

$$Re = \frac{n\rho_f D_p}{\mu_f} \|\mathbf{U}_s - \mathbf{U}_f\| \quad (26)$$

²⁷⁴ The function $F(\phi_s, Re)$ can be calculated as:

$$F(\phi_s, Re) = F(\phi_s, 0) + \frac{0.413Re}{24(1-\phi_s)^2} \left(\frac{(1-\phi_s)^{-1} + 3\phi_s(1-\phi_s) + 8.4Re^{-0.343}}{1 + 10^{3\phi_s} Re^{-(1+4\phi_s)/2}} \right) \quad (27)$$

²⁷⁵ where the low Reynold coefficient $F(\phi_s, Re \rightarrow 0)$ is:

$$F(\phi_s, 0) = \frac{10\phi_s}{(1-\phi_s)^2} + (1-\phi_s)^2(1 + 1.5\sqrt{\phi_s}) \quad (28)$$

²⁷⁶ When validating the model with analytical solution, it requires to know the
²⁷⁷ hydraulic conductivity K . In such case, we convert the equation (25) to
²⁷⁸ Kozeny-Carman formula by assuming $F(\phi_s, Re) = 10\phi_s/(1-\phi_s)^2$, ~~then the~~
²⁷⁹ leading to

$$\mathbf{f}_d = \frac{180\phi_s^2\mu_f}{D_p^2(1-\phi_s)} (\mathbf{U}_s - \mathbf{U}_f) \quad (29)$$

²⁸⁰ Then, the draging force following the Darcy law is given by:

$$\mathbf{f}_d = \frac{n^2\mu_f}{\kappa} (\mathbf{U}_s - \mathbf{U}_f) \quad (30)$$

²⁸¹ where κ being intrinsic permeability of soil which can be written as:

$$\kappa = \frac{K\mu_f}{\rho_f g} \quad (31)$$

²⁸² As such, the hydraulic conductivity will be expressed as $D_p^2(1-\phi_s)^3/180\mu_f\phi_s^2$.

²⁸³ \vdots

$$K = \frac{D_p^2(1-\phi_s)^3}{180\phi_s^2\mu_f} \rho_f g \quad (32)$$

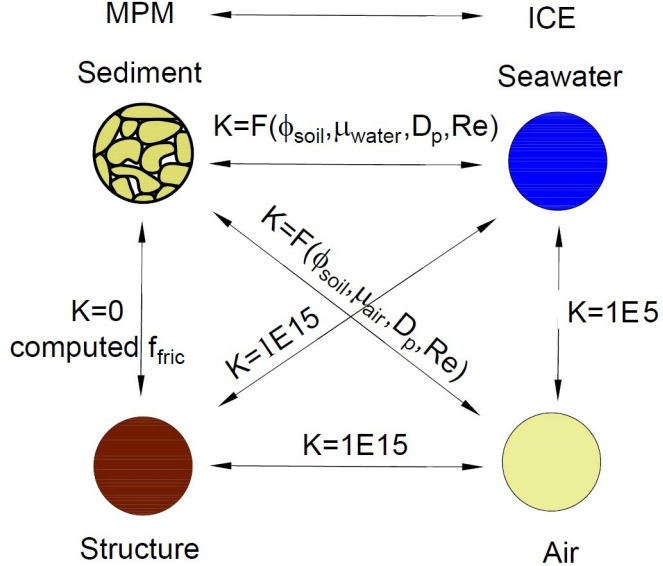


Figure 3: Momentum exchange coefficient between materials

284 Solving momentum and energy exchange with an implicit solver

285 The derivation of the implicit integration for the momentum exchange is
 286 presented in the Appendix's section 'Momentum and energy exchange with
 287 an implicit solver'. The linear equations for multi phases $i,j=1:N$ has the
 288 form [as](#):

$$\begin{vmatrix} (1 + \beta_{ij}) & -\beta_{ij} \\ -\beta_{ji} & (1 + \beta_{ji}) \end{vmatrix} \begin{vmatrix} \Delta \mathbf{U}_i \\ \Delta \mathbf{U}_j \end{vmatrix} = \begin{vmatrix} \beta_{ij} (\mathbf{U}_i^* - \mathbf{U}_j^*) \\ \beta_{ji} (\mathbf{U}_i^* - \mathbf{U}_j^*) \end{vmatrix}$$

289 where the intermediate velocity for fluid phases $f=1:N_f$ and for solid/porous
 290 phases $s=1:N_s$ can be calculated by:[_](#)

$$\begin{aligned} \mathbf{U}_f^* &= \mathbf{U}_f^n + \Delta t \left(-\frac{\nabla P_f^{n+1}}{\rho_f^n} + \frac{\nabla \cdot \boldsymbol{\tau}_f^n}{\bar{\rho}_f^n} + \mathbf{b} \right) \\ \mathbf{U}_s^* &= \mathbf{U}_s^n + \Delta t \left(\frac{\nabla \cdot \boldsymbol{\sigma}'^n}{\bar{\rho}_s^n} - \frac{\nabla P_f^{n+1}}{\rho_s} + \mathbf{b} \right) \end{aligned} \quad (33)$$

291 Also, the momentum exchange coefficient can be computed at every time
 292 step as $\beta_{12} = K/\bar{\rho}_f^n$ and $\beta_{21} = K/\bar{\rho}_s^n$ with the coefficient depending on the
 293 different type of interactions (see Figure 3) as for example:

294

- 295 1. The drag force is set to zero in soil-structure interactions, and instead
 296 the frictional force is computed.
 297 2. As a result of fluid-structure interaction, the momentum exchange coef-
 298 ficient should be extremely high (1E15) when the solid material points
 299 are considered to be zero-porosity/zero-permeability.
 300 3. In the case of soil-fluid interaction, the drag force is calculated using
 301 the equation (25). Considering that air has a much lower viscosity than
 302 water, its drag force is much lower than the drag force of water in a
 303 pore.
 304 4. A momentum exchange coefficient of 1E5 is applied between multiphase
 305 flows. This value is far higher than reality [21], but it is necessary to
 306 have enough numerical stability to conduct simulations in the numerical
 307 example.

308 Similar approach applied for the energy exchange term leading to:

$$\begin{vmatrix} (1 + \eta_{ij}) & -\eta_{ij} \\ -\eta_{ji} & (1 + \eta_{ji}) \end{vmatrix} \begin{vmatrix} \Delta T_i \\ \Delta T_j \end{vmatrix} = \begin{vmatrix} \eta_{ij}(T_i^n - T_j^n) \\ \eta_{ji}(T_j^n - T_i^n) \end{vmatrix}$$

309 with η ~~is being~~ the energy exchange coefficient.

310 *Equation of state for fluid phases*

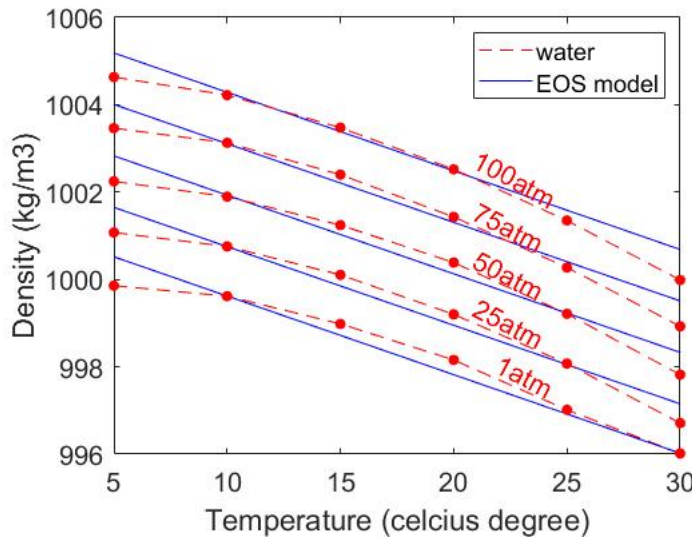


Figure 4: Equation of state of water

311 The equation of state establishes relations between thermodynamics vari-
 312 ables $[P_f, \rho_f, T_f]$. The choice of the equation of state depends on the types
 313 of the fluid materials. For example, for the air, it is possible to assume the
 314 equation of state for the perfect gas which obeys:

$$P_f = \rho_f R T_f \quad (34)$$

315 where R is the gas constant. For the water, a simple linear equation of state
 316 is in the following form:

$$P_f = P_{ref} + K_f(\rho_f - \rho_{ref}) \alpha_f(T_f - T_{ref}) \quad (35)$$

317 where reference pressure $P_{ref} = 1 \text{ atm} = 101325 \text{ Pa}$, reference temperature
 318 $T_{ref} = 10^\circ\text{C}$, reference density $\rho_{ref} = 999.8 \text{ kg/m}^3$, the bulk modulus of water
 319 $K_f = 2 \text{ GPa}$, and the water thermal expansion $\alpha_f = 0.18 \text{ }^\circ\text{C}^{-1}$. Equation
 320 (35) matches well with the state of the water (see Figure 4).

321 Numerical implementation

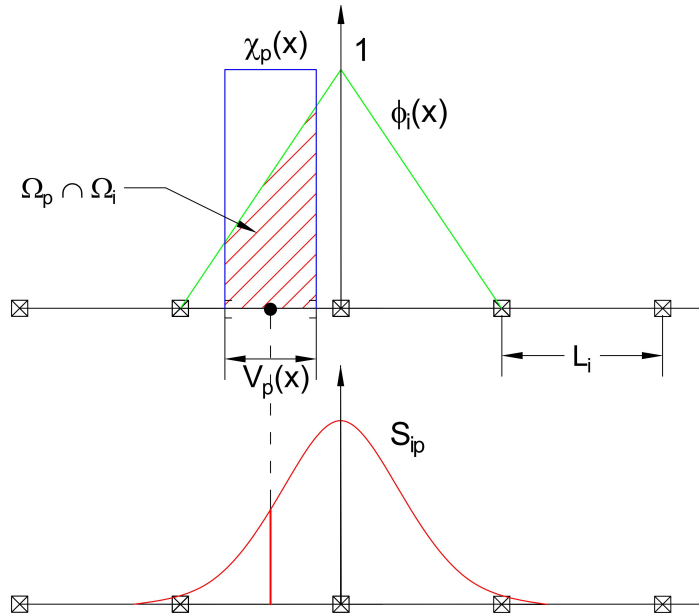


Figure 5: GIMP weighting function (red as a convolution of the linear basis shape function (green) and the charateristic-charateristic function (blue))

322 The fluid phases are discretized in the grid with the state variables stored
 323 at the centroid of the cells $[\rho_{fc}, \mathbf{U}_{fc}, T_{fc}, v_{fc}]$ while the
 324 solid phase is discretized in the particles with the state variables $[m_{sp}, \mathbf{U}_{sp}, T_{sp}, \boldsymbol{\sigma}'_{sp}]$.
 325 In the Material Point Method, we use the generalized interpolation technique
 326 [22] using the weight function as a convolution of a grid shape function $N_i(\mathbf{x})$
 327 in a nodal domain Ω_i and a characteristic function $\chi_p(\mathbf{x})$ in a particle domain
 328 Ω_p with the volume $V_p(\mathbf{x})$ as follows:

$$S_{ip} = \frac{1}{V_p} \int_{\Omega_i \cap \Omega_p} N_i(\mathbf{x}) \chi_p(\mathbf{x}) d\mathbf{x} \quad (36)$$

329 where the volume $V_p(\mathbf{x})$ of the material point p can be calculated as:

$$V_p = \int_{\Omega_p} \chi_p(\mathbf{x}) d\mathbf{x} \quad (37)$$

330 The ~~charateristic~~ characteristic function is the Heaviside function as $\chi_p =$
 331 1 if $\mathbf{x} \in \Omega_p$, otherwise 0 (see Figure 5). For the interpolation of the centroid
 332 of the cell, the linear basis function is used as:

$$S_{ci} = N_i(\mathbf{x}_c) \quad (38)$$

333 The time discretization are solved using the following steps:~~:-~~~

334 *Interpolation from Solid Particle to Grid*

335 The nodal values of the solid state (mass, velocity, temperature, volume)
 336 are:

$$\begin{aligned} m_{si}^n &= \sum S_{ip} m_{sp} \\ \mathbf{U}_{si}^n &= \frac{\sum S_{ip} (m\mathbf{U})_{sp}^n}{m_{si}^n} \\ T_{si}^n &= \frac{\sum S_{ip} (mT)_{sp}^n}{m_{si}^n} \\ V_{si}^n &= \frac{\sum S_{ip} (mV)_{sp}^n}{m_{si}^n} \\ \boldsymbol{\sigma}_{si}^n &= \frac{\sum S_{ip} (\boldsymbol{\sigma}V)_{sp}^n}{V_{si}^n} \end{aligned} \quad (39)$$

337 The nodal internal forces is calculated by:~~:-~~~

$$\mathbf{f}_{si}^{int,n} = - \sum \nabla S_{ip} (\boldsymbol{\sigma}'_{sp})^n V_{sp}^n \quad (40)$$

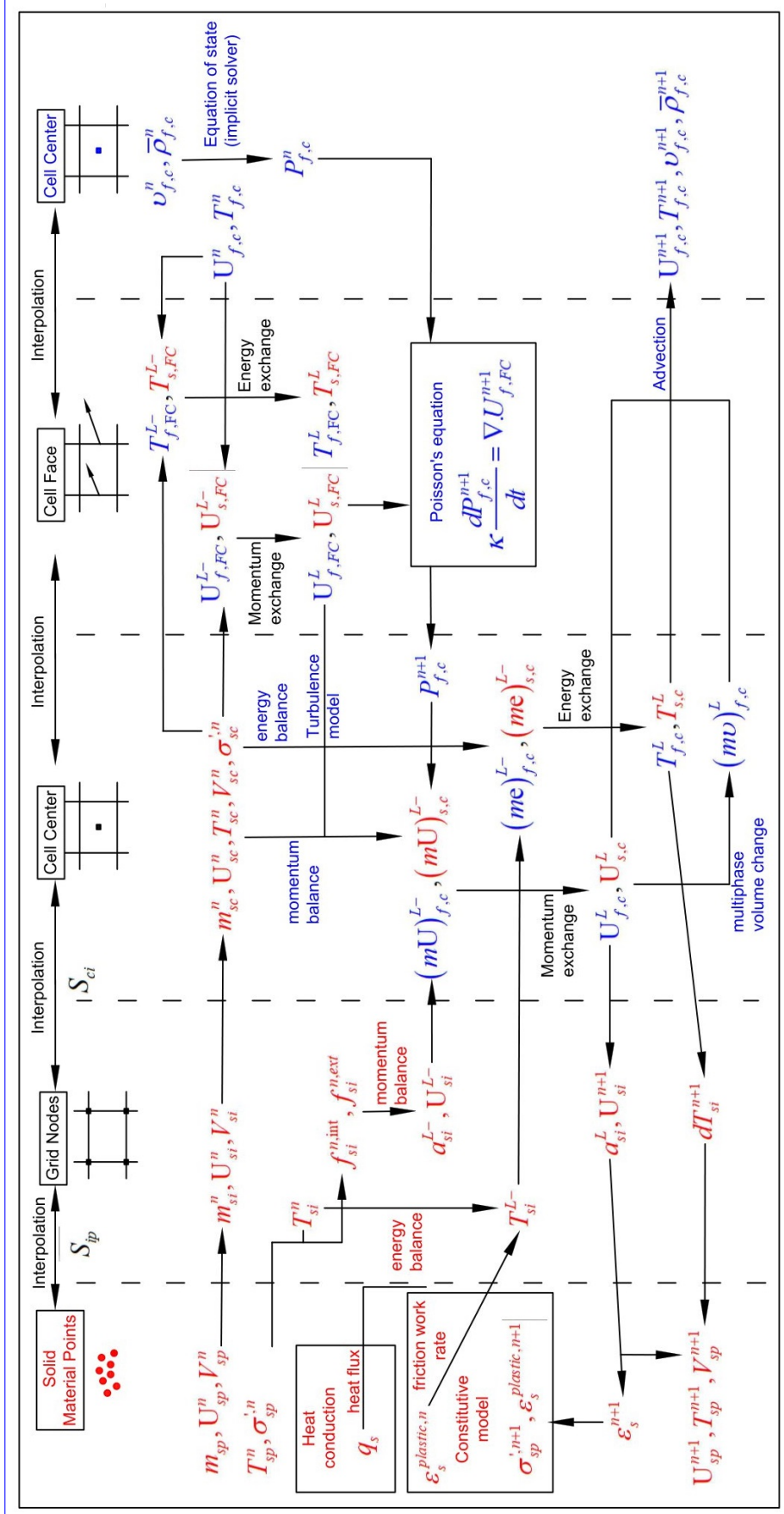


Figure 6: Numerical implementation of MPMCE

338 The nodal external forces $f_{si}^{ext,n}$ and extra momentum from contact forces the
 339 frictional forces from soil-structure interaction $f_{fric,si}^n$ from contact between
 340 materials are computed here. The nodal velocity and nodal temperature are
 341 applied boundary conditions.

342 Then we compute the solid cell variables as:

$$\begin{aligned} m_{sc}^n &= \sum S_{ci} m_{si} \\ \rho_{sc}^n &= \frac{m_{sc}^n}{V} \\ \mathbf{U}_{sc}^n &= \sum S_{ci} \mathbf{U}_{si}^n \\ T_{sc}^n &= \sum S_{ci} T_{si}^n \\ V_{sc}^n &= \sum S_{ci} V_{si}^n \\ \boldsymbol{\sigma}_{sc}^n &= \sum S_{ci} \boldsymbol{\sigma}_{si}^n \end{aligned} \quad (41)$$

343 Compute equation of state for fluid phase

344 Considering the total fluid material The total fluid material volume of a
 345 cell is:

$$V_{total} = \sum_{f=1}^{N_f} M_f v_f \quad (42)$$

346 Then we We need to find P_{eq} $P_{f,e}^n$ which allows each fluid materials obey their
 347 equation of states $[P_f, \rho_f, v_f, T_f, e_f]$ but also allow mass of all fluid materials
 348 to fill the entire the pore volume without ongoing compression or expansion
 349 following the condition as follows:

$$0 = n - \sum_{f=1}^{N_f} v_f \bar{\rho}_f \quad (43)$$

350 Then, we can use he the Newton-Raphson interation to find the value of P_{eq}
 351 $P_{f,e}^n$ which satisfies the equation (42, 43) and each equation of states of each
 352 fluid materials.

353 ~~Compute faced-centered velocity~~ Compute cell face velocity

354 Following the derivation in the Appendix: Advanced Fluid Pressure, we
 355 first compute the fluid ~~face-centered velocity~~ as cell face velocity as:

$$\mathbf{U}_{f,FC}^{*\underline{\mathbf{L}}\underline{-}} = \frac{(\bar{\rho}\mathbf{U})_{f,FC}^n}{\bar{\rho}_{f,FC}^n} + \Delta t \left(-\frac{\nabla^{FC} P_{eq}}{\rho_{f,FC}^n} \frac{\nabla^{FC} P_{f,c}^n}{\rho_{f,FC}^n} + \frac{\nabla^{FC} \cdot \boldsymbol{\tau}^n}{\bar{\rho}_{s,FC}} + \mathbf{b} \right) \quad (44)$$

356 The equation (44) is discretized in three dimension (noted that $\nabla^{FC} \cdot \boldsymbol{\tau} = 0$),
 357 for example the discretized equation in the x direction is:

$$U_{fx}^{L-} = \frac{(\bar{\rho}U)_{fx,R}^n + (\bar{\rho}U)_{fx,L}^n}{\bar{\rho}_{fx,L}^n + \bar{\rho}_{fx,R}^n} + \Delta t \left(-\frac{2(v_{fx,L}^n v_{fx,R}^n)}{v_{fx,L}^n + v_{fx,R}^n} \frac{P_{f,cx,R}^n - P_{f,cx,L}^n}{\Delta x} + b_x \right) \quad (45)$$

358 The ~~face-centered~~ cell face solid velocity can be calculated as:

$$\mathbf{U}_{s,FC}^{*\underline{\mathbf{L}}\underline{-}} = \frac{(\bar{\rho}\mathbf{U})_{s,FC}^n}{\bar{\rho}_{s,FC}^n} + \Delta t \left(\frac{\nabla^{FC} \cdot \boldsymbol{\sigma}_c'^n}{\bar{\rho}_{s,FC}^n} - \frac{\nabla^{FC} P_{eq}}{\rho_s} \frac{\nabla^{FC} P_{f,c}^n}{\rho_s} + \mathbf{b} \right) \quad (46)$$

359 The equation (46) is discretized in three dimension (noted that $\nabla^{FC} \cdot \boldsymbol{\sigma}_{ij} = 0$
 360 with $i \neq j$), for example the discretized equation in the x direction is:

$$U_{sx}^{L-} = \frac{(\bar{\rho}U)_{sx,R}^n + (\bar{\rho}U)_{sx,L}^n}{\bar{\rho}_{sx,L}^n + \bar{\rho}_{sx,R}^n} + \Delta t \left(\frac{2(\sigma_{xx,R} - \sigma_{xx,L})}{(\bar{\rho}_{sx,L}^n + \bar{\rho}_{sx,R}^n)\Delta x} - \frac{P_{f,cx,R}^n - P_{f,cx,L}^n}{\rho_s \Delta x} + b_x \right) \quad (47)$$

361 ~~Computing the modified faced-centered~~ Then, we compute the modified cell
 362 face velocity \mathbf{U}_{FC}^L considering the momentum exchange (see the Appendix:
 363 Momentum exchange with an implicit solve) as follows:

$$\begin{aligned} \mathbf{U}_{f,FC}^L &= \mathbf{U}_{f,FC}^{*\underline{\mathbf{L}}\underline{-}} + \Delta \mathbf{U}_{f,FC} \\ \mathbf{U}_{s,FC}^L &= \mathbf{U}_{s,FC}^{*\underline{\mathbf{L}}\underline{-}} + \Delta \mathbf{U}_{s,FC} \end{aligned} \quad (48)$$

364 ~~Solving the~~ The linear equation below is solved to obtain the increment of
 365 velocity with $i,j = 1 : N$ as:

$$\begin{vmatrix} (1 + \beta_{ij}) & -\beta_{ij} \\ -\beta_{ji} & (1 + \beta_{ji}) \end{vmatrix} \begin{vmatrix} \Delta \mathbf{U}_{i,FC} \\ \Delta \mathbf{U}_{j,FC} \end{vmatrix} = \begin{vmatrix} \beta_{ij} (\mathbf{U}_{i,FC}^{*\underline{\mathbf{L}}\underline{-}} - \mathbf{U}_{j,FC}^{*\underline{\mathbf{L}}\underline{-}}) \\ \beta_{ji} (\mathbf{U}_{j,FC}^{*\underline{\mathbf{L}}\underline{-}} - \mathbf{U}_{i,FC}^{*\underline{\mathbf{L}}\underline{-}}) \end{vmatrix}$$

366 ~~Compute faced-centered temperature~~ Compute cell face temperature

367 Similar to the velocity, the faced temperature is computed, for example
 368 in x direction, as:

$$\begin{aligned} \tilde{T}_{fx}^{\text{nL}\sim} &= \frac{(\bar{\rho}T)_{fx,R}^n + (\bar{\rho}T)_{fx,L}^n}{\bar{\rho}_{fx,L}^n + \bar{\rho}_{fx,R}^n} \\ \tilde{T}_{sx}^{L-} &= \frac{(\bar{\rho}T)_{sx,R}^n + (\bar{\rho}T)_{sx,L}^n}{\bar{\rho}_{sx,L}^n + \bar{\rho}_{sx,R}^n} \end{aligned} \quad (49)$$

369 ~~Computing the modified faced-centered~~ Then, we compute the modified cell
 370 face temperature T_{FC}^L considering the energy exchange (see the Appendix:
 371 Momentum and energy exchange with an implicit solver) as follows:

$$\begin{aligned} T_{f,FC}^L &= T_{f,FC} + \Delta T_{f,FC}^{\text{nL}\sim} \\ T_{s,FC}^L &= T_{s,FC} + \Delta T_{s,FC}^{\text{nL}\sim} \end{aligned} \quad (50)$$

372 ~~Solving the~~ The linear equation below ~~to obtain~~ is solved to determine the
 373 increment of velocity with $i,j = 1 : N$ as:

$$\begin{vmatrix} (1 + \eta_{ij}) & -\eta_{ij} \\ -\eta_{ji} & (1 + \eta_{ji}) \end{vmatrix} \begin{vmatrix} \Delta T_{i,FC} \\ \Delta T_{j,FC} \end{vmatrix} = \begin{vmatrix} \eta_{ij}(T_{i,FC}^{\text{nL}\sim} - T_{j,FC}^{\text{nL}\sim}) \\ \eta_{ji}(T_{j,FC}^{\text{nL}\sim} - T_{i,FC}^{\text{nL}\sim}) \end{vmatrix}$$

374 *Compute fluid pressure (implicit scheme)*

375 For single phase flow, the increment of the fluid pressure can be computed
 376 as:

$$\kappa_f \frac{\Delta P}{dt} = \nabla^c \cdot \mathbf{U}_{f,FC}^{n+1} \quad (51)$$

377 For multi-phase flows, the increment of the fluid pressure of the mixture can
 378 be computed as:

$$\kappa \frac{\Delta P}{dt} = \sum_{f=1}^{N_f} \nabla^c \cdot (\phi_{f,FC} \mathbf{U}_{f,FC})^{n+1} \quad (52)$$

379 where $\kappa = \sum_{f=1}^{N_f} (\phi_{f,FC} \kappa_f) / \sum_{f=1}^{N_f} (\phi_{f,FC})$. Then, the fluid pressure at cell
 380 center is:

$$P_c^{n+1} = P_{\text{eq}_c}^n + \Delta P_c^n \quad (53)$$

381 Finally, the ~~face-centered-cell face~~ advanced fluid pressure is:

$$P_{FC}^{n+1} = \left(\frac{P_{c,L}^{n+1}}{\bar{\rho}_{f,L}^n} + \frac{P_{c,R}^{n+1}}{\bar{\rho}_{f,R}^n} \right) / \left(\frac{1}{\bar{\rho}_{f,L}^n} + \frac{1}{\bar{\rho}_{f,R}^n} \right) = \left(\frac{P_{c,L}^{n+1} \bar{\rho}_{f,R}^n + P_{c,R}^{n+1} \bar{\rho}_{f,L}^n}{\bar{\rho}_{f,L}^n \bar{\rho}_{f,R}^n} \right) \quad (54)$$

382 *Compute viscous shear stress term of the fluid phase*

383 This part compute the viscous shear stress $\Delta(m\mathbf{U})_{fc,\tau}$ $\Delta(m\mathbf{U})_{f,\omega\tau}$ for a
 384 single ~~viscous~~viscous compressible Newtonian fluid and optionally shear stress
 385 induced by the turbulent model.

386 *Compute nodal internal temperature of the solid phase*

387 The nodal internal temperature rate is computed based on the heat con-
 388 duction model as below:

$$dT_{si}^{\textcolor{red}{LL-}} = \frac{(\Delta W_{si}^n + \Delta W_{fric,i}^n + \nabla^i \cdot \mathbf{q}_{si}^n)}{m_{si}^n c_v} \quad (55)$$

389 where $\Delta W_{si}^n = \sigma' : \frac{D_s(\epsilon_s^p)}{Dt}$ is the mechanical work rate computed from the
 390 constitutive model with ϵ_s^p is the plastic strain, $\Delta W_{fric,i}^n$ is the work rate
 391 ~~eompted~~computed from the contact law due to the frictional sliding between
 392 solid materials. The heat flux is $\mathbf{q}_s = \bar{\rho}_s \beta_s \nabla T_s$ with β_s being the thermal
 393 conductivity of the solid materials.

$$T_{si}^{\textcolor{red}{LL-}} = T_{si}^n + dT_{si}^{\textcolor{red}{LL-}} \quad (56)$$

394 *Compute and integrate acceleration of the solid phase*

395 After interpolating from material points to the nodes, the nodal acceler-
 396 ation and velocity are ~~calculate by~~calculated by:

$$\mathbf{a}_{si}^{L-} = \frac{\mathbf{f}_{si}^{int,n} + \mathbf{f}_{si}^{ext,n}}{m_{si}^n} + \mathbf{g} \quad (57)$$

$$\mathbf{U}_{si}^{L-} = \mathbf{U}_{si}^n + \mathbf{a}_{si}^{L-} \Delta t \quad (58)$$

398 *Compute Lagrangian value (mass, momentum and energy)*

399 For the fluid phase, the linear momentum rate, the energy rate are: $\textcolor{blue}{\sim}$

$$400 \quad \Delta(m\mathbf{U})_{\underline{\text{fc}}\underline{\text{f},c}} = Vn_c^n \nabla^c P_c^{n+1} + \Delta(m\mathbf{U})_{\underline{\text{fc}}\underline{\text{f},c},\tau} + V\bar{\rho}_{\underline{\text{fc}}\underline{\text{f},c}}^n g \quad (59)$$

$$401 \quad \Delta(me)_{\underline{\text{fc}}\underline{\text{f},c}} = Vn_c^n P_c^{n+1} \nabla^c \cdot \mathbf{U}_{f,FC}^* + \nabla^c \cdot \mathbf{q}_{\underline{\text{fc}}\underline{\text{f},c}}^n \quad (60)$$

402 The Lagrangian value of the mass, linear momentum and energy of fluid
403 phases without momentum exchange are: $\textcolor{blue}{\sim}$

$$404 \quad m_{\underline{\text{fc}}\underline{\text{f},c}}^L = V\bar{\rho}_{\underline{\text{fc}}\underline{\text{f},c}}^n \quad (61)$$

$$405 \quad (m\mathbf{U})_{\underline{\text{fc}}\underline{\text{f},c}}^{L-} = V\bar{\rho}_{\underline{\text{fc}}\underline{\text{f},c}}^n \mathbf{U}_{\underline{\text{fc}}\underline{\text{f},c}}^n + \Delta(m\mathbf{U})_{\underline{\text{fc}}\underline{\text{f},c}} \quad (62)$$

$$406 \quad (me)_{\underline{\text{fc}}\underline{\text{f},c}}^{L-} = V\bar{\rho}_{\underline{\text{fc}}\underline{\text{f},c}}^n T_{\underline{\text{fc}}\underline{\text{f},c}}^n c_v + \Delta(me)_{\underline{\text{fc}}\underline{\text{f},c}} \quad (63)$$

407 For the solid phase, the Lagrangian value of the linear momentum and energy
408 of solid phase are: $\textcolor{blue}{\sim}$

$$409 \quad m_{sc}^L = m_{sc}^n \quad (64)$$

$$410 \quad (m\mathbf{U})_{sc}^{L-} = \sum S_{ci} m_{si}^n \mathbf{U}_{si}^{L-} + V(1 - n_c^n) \nabla^c P_{\underline{\text{fc}}\underline{\text{f},c}}^{n+1} \quad (65)$$

$$411 \quad (me)_{sc}^{L-} = \sum S_{ci} m_{si}^n T_{si}^L c_v \quad (66)$$

412 To consider the momentum exchange, the Lagrangian velocity is modified as: $\textcolor{blue}{\sim}$

$$413 \quad \begin{aligned} \mathbf{U}_{\underline{\text{fc}}\underline{\text{f},c}}^L &= \mathbf{U}_{\underline{\text{fc}}\underline{\text{f},c}}^{L-} + \Delta\mathbf{U}_{\underline{\text{fc}}\underline{\text{f},c}} \\ \mathbf{U}_{sc}^L &= \mathbf{U}_{sc}^{L-} + \Delta\mathbf{U}_{sc} \end{aligned} \quad (67)$$

414 where the cell-centered intermediate velocity can be calculated by: $\textcolor{blue}{\sim}$

$$415 \quad \begin{aligned} \mathbf{U}_{\underline{\text{fc}}\underline{\text{f},c}}^{L-} &= \frac{(m\mathbf{U})_{fc}^{L-}}{m_{fc}^L} \frac{(m\mathbf{U})_{f,c}^{L-}}{m_{f,c}^L} \\ \mathbf{U}_{sc}^{L-} &= \frac{(m\mathbf{U})_{sc}^{L-}}{m_{sc}^L} \end{aligned} \quad (68)$$

412 And the increment of the velocity $\mathbf{U}_{fc} \mathbf{U}_{fc}$, $\Delta \mathbf{U}_{sc}$ can be computed by solving
 413 the linear equation with $i,j = 1:N$ as:

$$\begin{vmatrix} (1 + \beta_{ij}) & -\beta_{ij} \\ -\beta_{ji} & (1 + \beta_{ji}) \end{vmatrix} \begin{vmatrix} \Delta \mathbf{U}_{i,c} \\ \Delta \mathbf{U}_{j,c} \end{vmatrix} = \begin{vmatrix} \beta_{ij} (\mathbf{U}_{i,c}^{*L-} - \mathbf{U}_{j,c}^{*L-}) \\ \beta_{ji} (\mathbf{U}_{j,c}^{*L-} - \mathbf{U}_{i,c}^{*L-}) \end{vmatrix}$$

414 To consider the energy exchange, the Lagrangian temperature is modified as:
 415

$$\begin{aligned} T_{fcLc}^L &= T_{fcLc}^{L-} + \Delta T_{fcLc} \\ T_{sc}^L &= T_{sc}^{L-} + \Delta T_{sc} \end{aligned} \quad (69)$$

416 where the cell-centered intermediate temperature can be calculated by:
 417

$$\begin{aligned} T_{fcLc}^{L-} &= \frac{(mT)_{fc}^{L-}}{\underline{m_{fc}^L c_v}} \frac{(mT)_{f,c}^{L-}}{\underline{m_{f,c}^L c_v}} \\ T_{sc}^{L-} &= \frac{(mT)_{sc}^{L-}}{\underline{m_{sc}^L c_v}} \end{aligned} \quad (70)$$

417 And the increment of the velocity can be computed by solving the linear
 418 equation with $i,j = 1:N$ as:

$$\begin{vmatrix} (1 + \eta_{ij}) & -\eta_{ij} \\ -\eta_{ji} & (1 + \eta_{ji}) \end{vmatrix} \begin{vmatrix} \Delta T_{i,c} \\ \Delta T_{j,c} \end{vmatrix} = \begin{vmatrix} \eta_{ij} (T_{i,c}^{nL-} - T_{j,c}^{nL-}) \\ \eta_{ji} (T_{j,c}^{nL-} - T_{i,c}^{nL-}) \end{vmatrix}$$

419 Finally, we obtain the cell-centered solid acceleration and temperature rate
 420 as:
 421

$$d\mathbf{U}_{sc}^L = \frac{(m\mathbf{U})_{sc}^L - (m\mathbf{U})_{sc}^n}{m_{sc}^L \Delta t} \quad (71)$$

$$dT_{sc}^L = \frac{(me)_{sc}^L - (me)_{sc}^n}{m_{sc}^L c_v \Delta t} \quad (72)$$

422 Compute Lagrangian specific volume of the fluid phase

423 To compute the Lagrangian value of the specific volume of the fluid phase,
 424 we need to compute the Lagrangian temperature rate as below:
 425

$$T_{fcLc}^{n+1} = \frac{(me)_{fc}^L}{\underline{m_{fc}^L c_v}} \frac{(me)_{f,c}^L}{\underline{m_{f,c}^L c_v}} \quad (73)$$

425

$$\frac{D_f T_{fc}}{Dt} \frac{D_f T_{f,c}}{Dt} = \frac{T_{fc}^{n+1} - T_{fc}^n}{\Delta t} \frac{T_{f,c}^{n+1} - T_{f,c}^n}{\Delta t} \quad (74)$$

426 As such, the Lagrangian specific volume rate is:

$$\Delta(mv)_{\underline{\underline{fcfc}}} = V f_{\underline{\underline{fcfc}}}^\phi \nabla \cdot \mathbf{U} + (\phi_{\underline{\underline{fcfc}}} \alpha_{\underline{\underline{fcfc}}} \frac{D_f T_{fc}}{Dt} \frac{D_f T_{f,c}}{Dt}) - f_{\underline{\underline{fcfc}}}^\phi \sum_{n=1}^N \phi_{nc} \alpha_{nc} \frac{D_n T_{nc}}{Dt} \frac{D_n T_{n,c}}{Dt} \quad (75)$$

427 where $f_f^\phi = (\phi_f \kappa_f) / (\sum_{n=1}^N \phi_n \kappa_n)$ and $\mathbf{U} = \nabla \cdot (\sum_{s=1}^{N_s} \phi_{sc} \mathbf{U}_{sc} + \sum_{f=1}^{N_f} \phi_{fc} \mathbf{U}_{fc})$

428 Finally, the Lagrangian specific volume is:

$$(mv)_{\underline{\underline{fcfc}}}^L = V \bar{\rho}_{f,c}^n v_{\underline{\underline{fcfc}}}^n + \Delta(mv)_{\underline{\underline{fcfc}}} \quad (76)$$

429 *Compute advection term and advance in time*

430 The time advanced mass, linear momentum, energy and specific volume
431 are:

$$m_{\underline{\underline{fcfc}}}^{n+1} = m_{\underline{\underline{fcfc}}}^L - \Delta t \nabla \cdot (\bar{\rho}_{\underline{\underline{fcfc}}}^L, \mathbf{U}_{f,FC}^L) \quad (77)$$

$$(m\mathbf{U})_{\underline{\underline{fcfc}}}^{n+1} = (m\mathbf{U})_{\underline{\underline{fcfc}}}^L - \Delta t \nabla \cdot ((\bar{\rho}\mathbf{U})_{\underline{\underline{fcfc}}}^L, \mathbf{U}_{f,FC}^L) \quad (78)$$

$$(me)_{\underline{\underline{fcfc}}}^{n+1} = (me)_{\underline{\underline{fcfc}}}^L - \Delta t \nabla \cdot ((\bar{\rho}c_v T)_{\underline{\underline{fcfc}}}^L, \mathbf{U}_{f,FC}^L) \quad (79)$$

$$(mv)_{\underline{\underline{fcfc}}}^{n+1} = (mv)_{\underline{\underline{fcfc}}}^L - \Delta t \nabla \cdot ((\bar{\rho}v)_{\underline{\underline{fcfc}}}^L, \mathbf{U}_{f,FC}^L) \quad (80)$$

435 Finally, the state variables of the fluid phases of the next time step are:

$$\bar{\rho}_{\underline{\underline{fcfc}}}^{n+1} = \frac{m_{fc}^{n+1}}{V} \frac{m_{f,c}^{n+1}}{V} \quad (81)$$

$$\mathbf{U}_{\underline{\underline{fcfc}}}^{n+1} = \frac{(m\mathbf{U})_{fc}^{n+1}}{m_{fc}^{n+1}} \frac{(m\mathbf{U})_{f,c}^{n+1}}{m_{f,c}^{n+1}} \quad (82)$$

$$T_{\underline{\underline{fcfc}}}^{n+1} = \frac{(me)_{fc}^{n+1}}{m_{fc}^{n+1}} \frac{(me)_{f,c}^{n+1}}{m_{f,c}^{n+1}} \quad (83)$$

$$v_{\underline{\underline{fcfc}}}^{n+1} = \frac{(mv)_{fc}^{n+1}}{m_{fc}^{n+1}} \frac{(mv)_{f,c}^{n+1}}{m_{f,c}^{n+1}} \quad (84)$$

439 *Interpolate from cell to node of the solid phase*

440 First we interpolate the acceleration, velocity and temperature rate to
441 the node as below:

$$442 \quad \mathbf{a}_{si}^n = \sum S_{ci} d\mathbf{U}_{sc}^L \quad (85)$$

$$443 \quad \mathbf{U}_{si}^{n+1} = \sum S_{ci} d\mathbf{U}_{sc}^L \Delta t \quad (86)$$

$$444 \quad dT_{si}^n = \sum S_{ci} dT_{sc}^L \quad (87)$$

444 Then the boundary condition and contact forces f_{si}^{fric} are applied to the
445 nodal velocity ~~and the acceleration is modified by, and then accelerations are~~
446 ~~modified by:~~

$$447 \quad \mathbf{a}_{si}^n = \frac{\mathbf{v}_{si}^{n+1} - \mathbf{v}_{si}^n}{\Delta t} \quad (88)$$

447 *Update the particle variables*

448 The state variables of the solid phase $[\mathbf{U}_{sp}^{n+1}, \mathbf{x}_{sp}^{n+1}, \nabla \mathbf{U}_{sp}^{n+1}, T_{sp}^{n+1}, \nabla T_{sp}^{n+1}, \mathbf{F}_{sp}^{n+1}, V_{sp}^{n+1}]$
449 (velocity, position, velocity gradient, temperature, temperature gradient, de-
450 formation gradient, volume) are updated ~~here as:~~

$$451 \quad \mathbf{U}_{sp}^{n+1} = \mathbf{U}_{sp}^n + \sum S_{sp} \mathbf{a}_{si}^n \Delta t \quad (89)$$

$$452 \quad \mathbf{x}_{sp}^{n+1} = \mathbf{x}_{sp}^n + \sum S_{sp} \mathbf{U}_{si}^{n+1} \Delta t \quad (90)$$

$$453 \quad \nabla \mathbf{U}_{sp}^{n+1} = \sum \nabla S_{sp} \mathbf{U}_{si}^{n+1} \quad (91)$$

$$454 \quad T_{sp}^{n+1} = T_{sp}^n + \sum S_{sp} dT_{si}^n \Delta t \quad (92)$$

$$455 \quad \nabla T_{sp}^{n+1} = \sum \nabla S_{sp} T_{sp}^n \Delta t \quad (93)$$

$$456 \quad \mathbf{F}_{sp}^{n+1} = (\mathbf{I} + \nabla \mathbf{U}_{sp}^{n+1} \Delta t) \mathbf{F}_{sp}^n \quad (94)$$

$$457 \quad V_{sp}^{n+1} = \det(\mathbf{F}_{sp}^{n+1}) V_{sp}^o \quad (95)$$

457 Finally, the effective stress $(\sigma')^{n+1}$ is updated from the constitutive model
458 and the pore water pressure is interpolated from the cell as:

$$459 \quad p_f^{n+1} = \sum S_{si} P_c^{n+1} \quad (96)$$

459 **Numerical examples**

460 All input files and the analytical calculations in this section are provided
 461 in the Github repository (https://github.com/QuocAnh90/Uintah_NTNU)
 462 for the reproduction of the numerical results.

463 To prevent repetition, we present the parameters of water and air, which
 464 remain consistent across all simulations. The water has a bulk modulus of 2
 465 GPa, a density of 998 kg/m³ at a reference temperature of 5 degrees Celsius
 466 and a reference pressure of 10325 Pa (1atm), a dynamic viscosity μ_f of 1
 467 mPa s). The air has a ideal gas with a density of 1.17 kg/m³ at a reference
 468 temperature of 5 degrees Celsius and a reference pressure of 10325 Pa (1atm),
 469 a dynamic viscosity μ_f of $18.45E^{-3}$ mPa s).

470 *Fluid Flow through isothermal porous media*

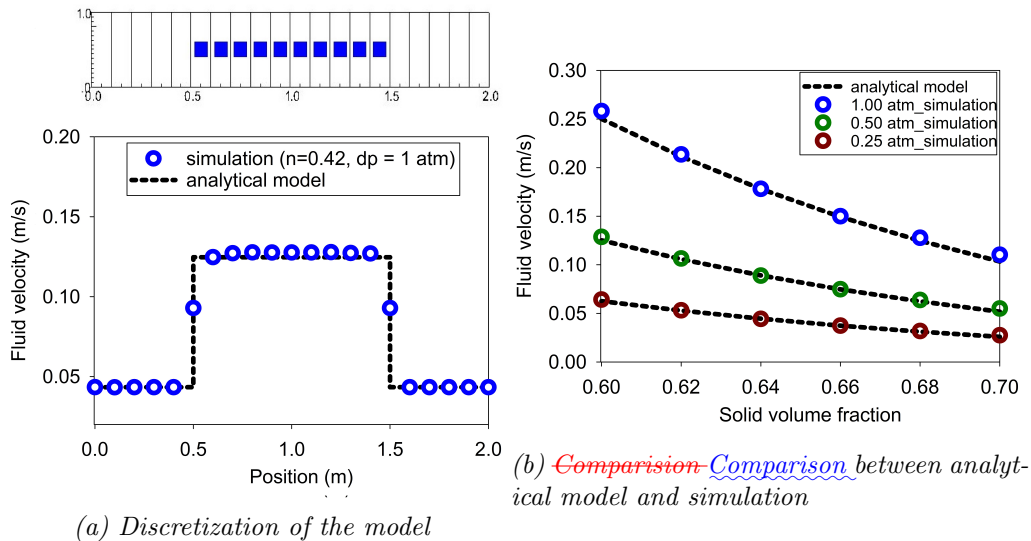


Figure 7: Numerical results of the fluid flow through isothermal porous media

471 Fluid flow through porous media is important in many engineering disci-
 472 plines, like predicting water flow in soil. Fluid flow velocity in one dimension
 473 can be calculated from the porous media's hydraulic conductivity K as:

474

$$U_f = K \frac{\Delta p_f}{L} \quad (97)$$

475 If the Carman-Kozeny formula is adopted $F = 10\phi_s/(1 - \phi_s)^2$, the hydraulic
 476 conductivity will be expressed as $K = d^2(1 - \phi_s)^3/180\mu\phi_s^2$.
 477 Then, the analytical formula of average velocity in one dimension through
 478 the porous media is:
 479

$$U_f = \frac{1}{n} \frac{d^2(1 - \phi_s)^3}{180\mu\phi_s^2} \frac{D_p^2(1 - \phi_s)^3}{180\phi_s^2\mu_f} \frac{\Delta p_f}{L} \quad (98)$$

480 Our numerical model is validated by modeling fluid flow through a 1m
 481 long porous media. This fluid has water properties (bulk modulus is 2GPa,
 482 density is 998 kg/m³ at 5 degrees Celsius and 10325 Pa (1atm) pressure,
 483 dynamic viscosity μ is 1mPa s). The porous media is modeled by elastic
 484 material with Young's modulus is 10 MPa, Poisson's ratio is 0.3, and density
 485 is 2650 kg/m³. The volume fraction of porous media ϕ_s is [0.6, 0.62, 0.66,
 486 0.68, 0.7] and the average grain diameter d is 1mm. The model is discretized
 487 in 20 finite element and the porous media in 10 finite element with 1 material
 488 point per element. The pressure gradient is applied with three different value
 489 [0.25, 0.5, 1] atm. Figure 7 shows a good agreement of fluid flow prediction
 490 between the theory and the model.

491 *Isothermal consolidation*

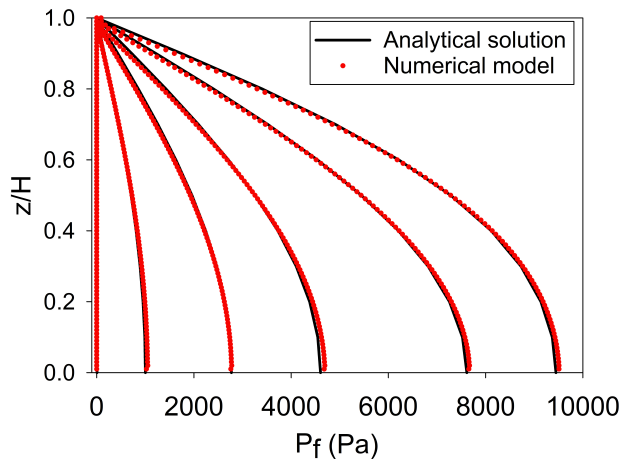


Figure 8: Comparison between analytical solution and numerical solution

492 A common benchmark ~~for~~ for a fully saturated porous ~~meida~~media is
 493 the simulation of one-dimensional consolidation. Using the Carman-Kozeny
 494 formula, the time-dependent pressure can be ~~evaluated~~calculated as:

$$p_f = \sum_{m=1}^{\infty} \frac{2F_{ext}}{M} \sin\left(\frac{Mz}{H}\right) e^{-M^2 T_v} \text{ with } M = \frac{\pi}{2}(2m+1) \quad (99)$$

495 where the consolidation rate $T_v = C_v t / H^2$, the consolidation coefficient $C_v =$
 496 $E_v n^3 d^2 / (180(1-n)^2 \mu)$ and the Oedometer modulus $E_v = E(1-v)/(1+v)/(1-2v)$. Our numerical model is validated by modeling the consolidation
 497 of a 1m column. ~~This fluid has water properties (bulk modulus is 2GPa,
 498 density is 998 kg/m3 at 5 degrees Celsius and 101325 Pa (1atm) pressure,
 499 dynamic viscosity μ is 1mPa s).~~ The porous media is modeled by elastic
 500 material with Young's modulus is 10 MPa, Poisson's ratio is 0.3, and density
 501 is 2650 kg/m3. The volume fraction of porous media ϕ_s is 0.7 which is
 502 equivalent to the porosity of 0.3 and the average grain diameter d is 1mm.
 503 The model is discretized in 100 finite element with 1 material point per
 504 element. The external pressure applies to the top of the column is 10 kPa.
 505 Figure 8 shows a good agreement of fluid flow prediction between the theory
 506 and the model.

508 *Thermal induced cavity flow*

509 Another ~~benchmark~~benchmark is the thermal induced cavity flow in
 510 porous media. Temperature and velocity distributions are calculated for a
 511 square non-deformable saturated porous media. The top and bottom walls
 512 are insulated, and the left and right walls are at fixed ~~temperatures differing
 513 by temperature gradient of~~ 1 degree. The fluid motion at steady state are
 514 cavity flow due to the temperature induced density variation. The numerical
 515 is validated by comparing with the numerical solution of the finite element
 516 method. The ~~fluid has water properties (bulk modulus is 2GPa, density is 998
 517 kg/m3 at 5 degrees Celsius and 10325 Pa (1atm) pressure, dynamic viscosity
 518 μ is 1 mPa s)~~. The porous media is modeled by non deformable material,
 519 and density is 2500 kg/m3. The specific heat capacity of the water and
 520 porous skeleton are 4181 J/kg.K and 835 J/kg.K respectively. The thermal
 521 conductivity of the water and porous skeleton are 0.598 W/m.K and 0.4
 522 W/m.K. The volume fraction of porous media ϕ_s is 0.6 which is equivalent
 523 to the porosity of 0.4 and the average grain diameter d is 1mm. The model is
 524 discretized in 20 x 20 finite element with 4 material point per element. Figure

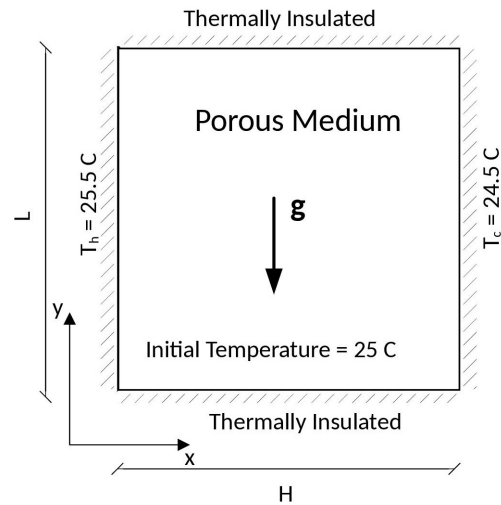


Figure 9: Model schematic [23]

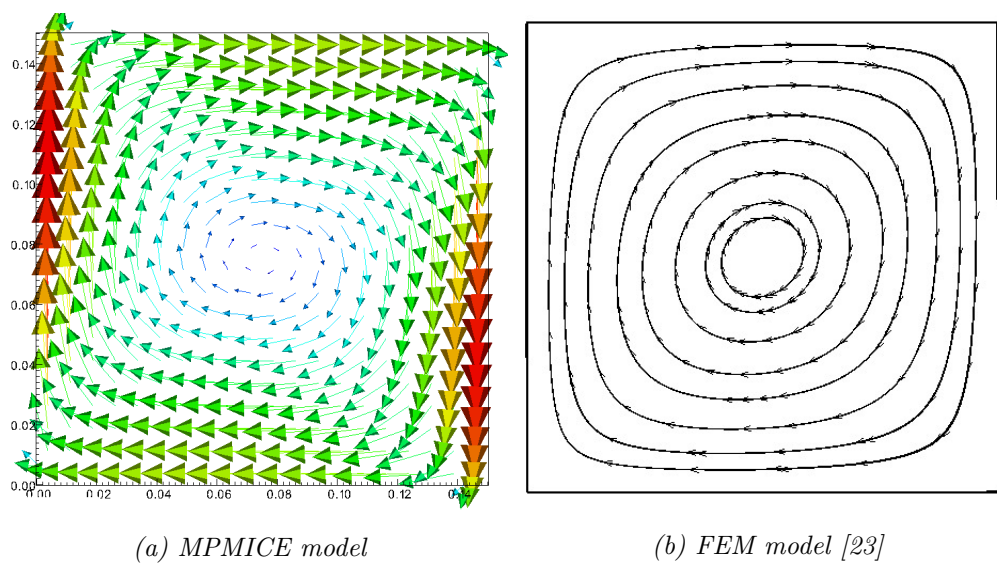


Figure 10: ~~Comparision~~ Comparison between MPMICE model and FEM model

525 10 shows a good agreement of numerical results of the model compared with
 526 the numerical solution of the finite element method.

527 *Underwater debris flow*

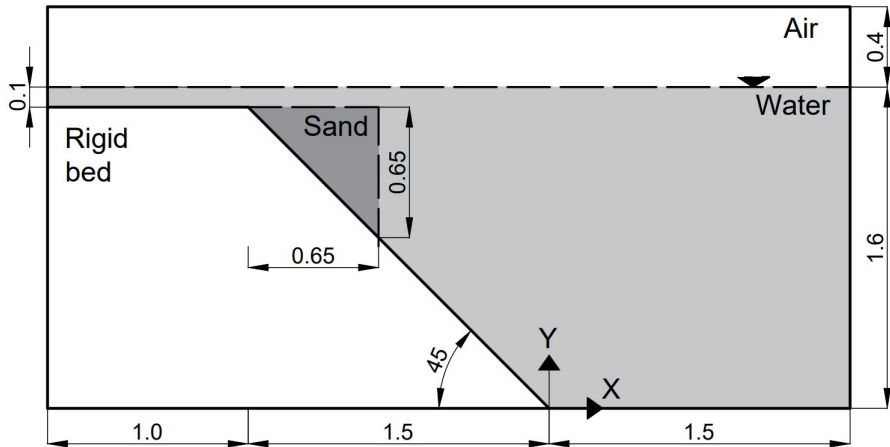


Figure 11: Model schematic

528 The numerical example is validated by using the experimental work of
 529 Rzadkiewicz et al. 's experiment on submarine debris flow [24]. During
 530 the In their experiment, sand in within a triangular box is released and then
 531 slides along a rigid bed inclined at 45 degrees under water -(see Figure 11-0.4
 532 seconds subfigure0.8 seconds subfigureSimulation of underwater debris flow
 533 figureMaterials Bulk modul(Pa)tabular Shear modul(Pa)tabular Density(kg/m³)tabula
 534 Temp(C)tabular Dynamic viscosity(Pa·s)tabular Yield stress(Pa)tabular
 535 Water(at surface)tabular2.15e9-999.85855e-6-Air(at top boundary)tabular-
 536 -1.177518.45e-6-Sand(porous media)tabular8.33e6 20e6 1985 5-200 Rigid
 537 bed(solid)tabular117e7 43.8e7 8900 5--tabularNumerical parameters for the
 538 underwater submarine debris tableIn-). The material properties in the nu
 539 mercial model ,the material properties are selected based on the experiment
 540 by Rzadkiewicz et al[24]. Sand has . [24]. The sand is characterized by a
 541 saturated density of 1985 kg/m³ and yield stress of 200 Pa. a friction angle
 542 of 10 degrees. The effect of Young's modulus has little effect on debris flow
 543 run-out because of the extreme large is negligible due to the extreme defor
 544 mation of the debris. Therefore, we select 50 MPa , so a Young's modulus
 545 with 0.25 of 50 MPa with a Poisson's ratio of 0.25 is chosen. The rigid bedis
 546 much stifferwith , being much stiffer, has bulk modulus and shear modulus

547 values of $117E^7$ Pa and $43.8E^7$ Pa. Under gravity, the density of the water
548 at the surface is 999.8 kg/m^3 at the pressure of 1 atm. At the top boundary,
549 the air has a density of 1.17 kg/m^3 at the atmospheric pressure of 1 atm.
550 At 5 Celsius degrees, air and water have viscosity of $18.45E^{-3}$ mPa s and
551 1 mPa s , respectively. The numerical parameters used in this example are
552 presented in Table 1.

553 On The boundary conditions imposed in the numerical model are as follows:
554 on all boundary faces, the Dirichlet boundary condition is imposed for velocity
555 (u -velocity is set to zero ($U = 0 \text{ m/s}$) and temperature the temperature is
556 set to 5 degrees Celsius ($T = 5 \text{ Celsius degrees}$), while the Neuman boundary
557 condition is imposed at the top boundary for pressure ($^\circ\text{C}$). At the top boundary,
558 the pressure has a Neumann boundary condition of $d\bar{p}/dx = 0 \text{ kPa}$) and
559 density (, and the density has a Neumann boundary condition of $d\rho/dx =$
560 0 kg/m^3). For the background mesh , there are . The background mesh
561 consists of $700 \times 400 = 280,000$ cells. In each cell of cells, resulting in a total
562 of 280,000 cells. Each cell in the debris flow and rigid bed , there are contains
563 2 x 2 material points.

564 0.4 seconds subfigure0.8 seconds subfigureSimulation of underwater debris
565 flow figureFigure ?? and ?? show Figure 13b illustrates snapshots of the
566 underwater debris flow sliding in the plane at 0.4 s and 0.8 s. Our simulations
567 match the computed results from Rzałkiewicz et al. [24]. The model also
568 captures , demonstrating that the model captures the typical hydroplaning
569 mechanism of the underwater debris flow(hydroplaning means the debris
570 flow is lifted up and no longer in . Hydroplaning refers to the lifting of the
571 debris flow, causing it to lose contact with the bottom layer). The elevation
572 of the free surface at 0.4s and 0.8s is compared between our proposed
573 method and other methods in Figure 12. Once again, our computed results
574 were consistent with both the experiment and others computational Our
575 computed results align well with the experimental results [7].

576 Unlike other computational models based that rely on total stress analysis
577 , the proposed model based on the [5, 6, 7, 8], our proposed model utilizes
578 effective stress analysiswhich allows to analyze the , enabling the analysis
579 of water pressure and temperature in within the debris flow. saturated
580 debris flow using MPM subfigureunderwater debris flow using MPMICE
581 subfigureSimulation of underwater debris flow figureWe also explore the difference
582 Additionally, we investigate the differences between underwater debris flow
583 and saturated debris flow in terms of interacting with obstacle their interaction
584 with obstacles. Figure 13 shows the snapshot of the simulations of presents

585 snapshots of simulations of both underwater and saturated debris flow. The
 586 saturated debris flow (see Figure 13a) behaves like frictional flow as grain
 587 exhibits behavior similar to frictional flow, where grains have contact forces
 588 with each other. On the other hand Conversely, the underwater debris flow
 589 (see Figure 13b) behaves like turbulent flow as grains are turbulent flow, with
 590 grains being separated from each other and exhibit exhibiting no contact
 591 forces between grains. (as reflected by the near-zero effective stress in the
 turbulence domain).

Materials	Bulk modul (Pa)	Shear modul (Pa)	Density (kg/m3)	Temp (C)	Dynamic viscosity (Pa s)	Friction angle (degrees)
Water (at surface)	2.15e9	-	999.8	5	855e-6	-
Air (at top boundary)	-	-	1.177	5	18.45e-6	-
Sand (porous media)	8.33e6	20e6	1985	5	-	10
Rigid bed (solid)	117e7	43.8e7	8900	5	-	-

Table 1: Numerical parameters for the underwater submarine debris

592

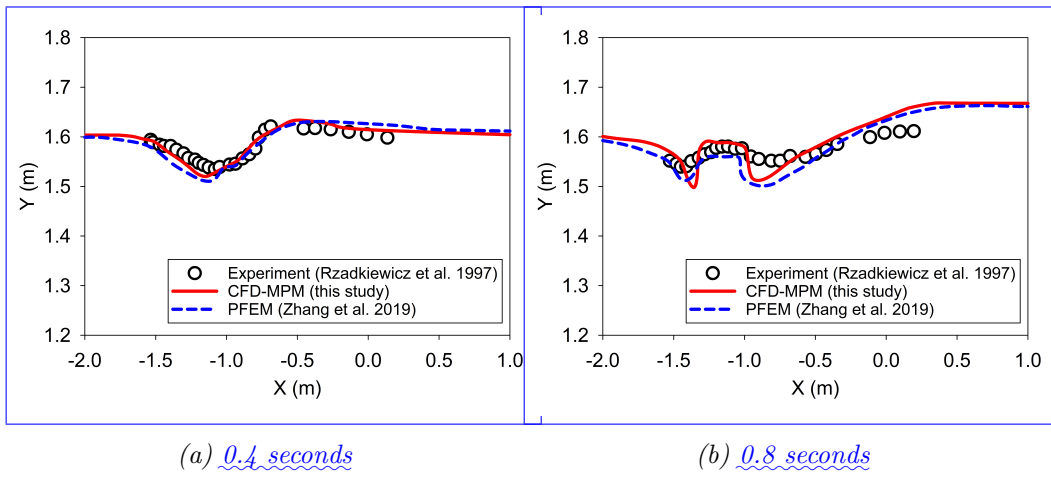


Figure 12: Evolution of water level in the simulation of underwater debris flow

593 Validation of soil response to the seismic loading

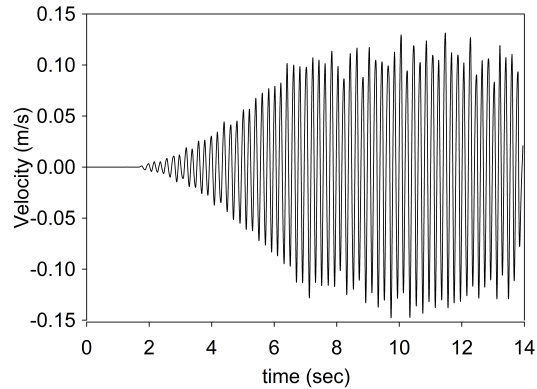


Figure 14: Seismic loading

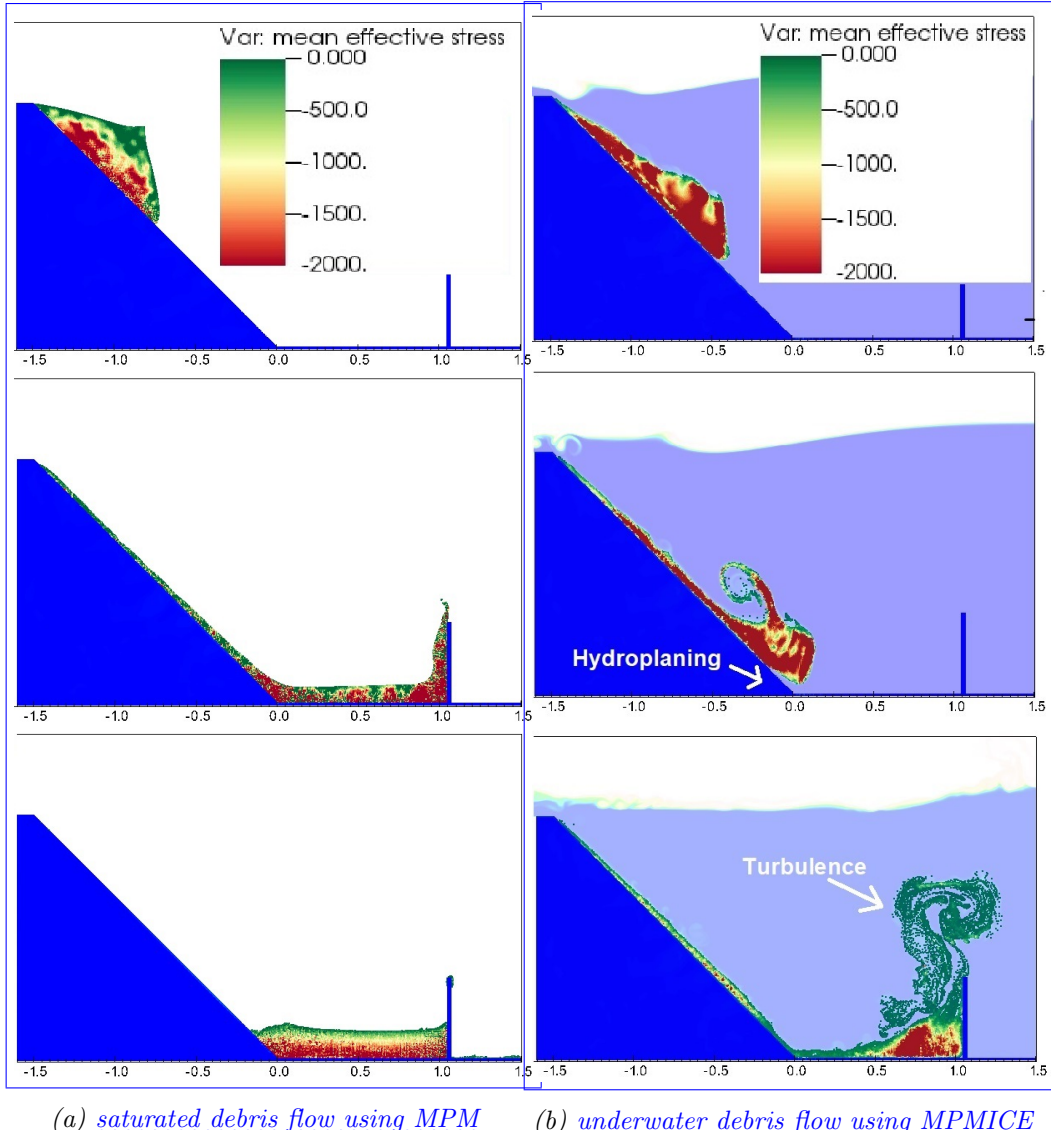


Figure 13: Simulation of Debris Flow: Mean Effective Stress Distribution (Green Color Indicates Near-Zero Effective Stress)

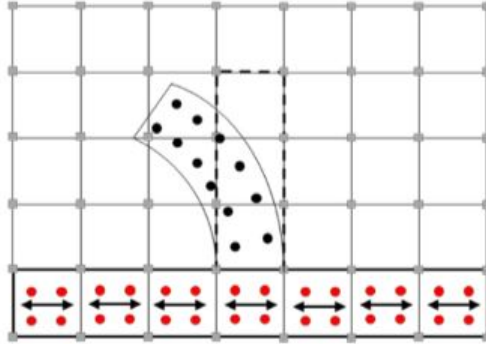


Figure 15: Material points prescribed velocity as kinematic boundary condition [25]

594 An experimental study conducted by Hiraoka et al. [26] aimed to investigate
 595 the influence of seismic shaking on the deformation of a 0.5 m-high sand slope.
 596 The sand used in the experiment was partially saturated, with a moisture
 597 content of 10 percent. The provided soil parameters for the Mohr Coulomb
 598 model include the effective friction angle of 23 degrees, apparent cohesion
 599 of 0.78 kPa, Young's modulus of 2.57 MPa, and Poisson's ratio of 0.33, and
 600 moist unit weight of 16.5 kN/m³. The soil's dilatancy angle was assumed to
 601 be 0 [26]. The experimental setup consisted of a shaking table box with a
 602 steel horizontal base and smooth glass vertical sidewalls. Laser sensors were
 603 used to monitor the displacement of the slope's toe and crest. Figure 14
 604 displays the velocity-time history employed in the experiment.

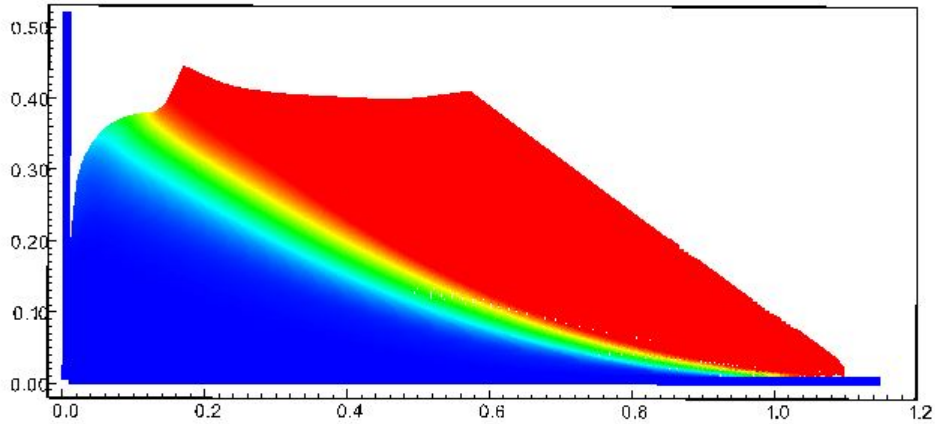


Figure 16: Numerical model of the seismic-induced slope failure with displacement color

To simulate the seismic loading in our numerical model, we adopted a method presented by Alsardi et al. [25], which involves specifying the velocity at the corresponding material points representing either the shaking table or the bedrock at the site (see Figure 15). In our simulation, we considered the horizontal base to be fully rough and the vertical contact to be fully smooth. The initial stress condition was initiated using gravity and seismic loading induced the slope failure (see Figure 16). Previous studies by Bhandari et al. [27], Alsardi et al. [25], and Hiraoka et al. [26] attempted to model this experiment using MPM and SPH models. In this study, we compared our results with those obtained from other particle-based methods (Figure 17). The main difference is that we did not apply 5 percent numerical damping in our model, unlike the other methods. We found that the final displacement of the slope toe in our MPM model was higher than that observed in the experiment. Nevertheless, the validation of the Mohr-Coulomb model under seismic response demonstrated a reasonable soil behavior in terms of displacement.

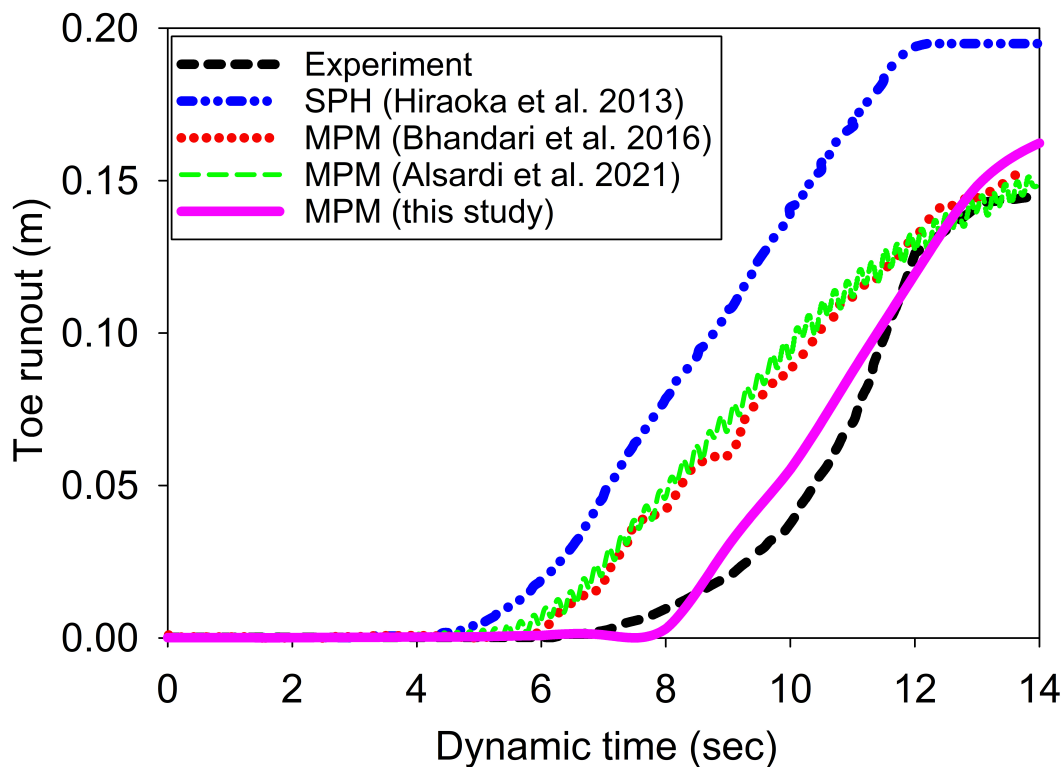


Figure 17: Displacement of the toe of the slope

621 *Earthquake-induced submarine landslides*

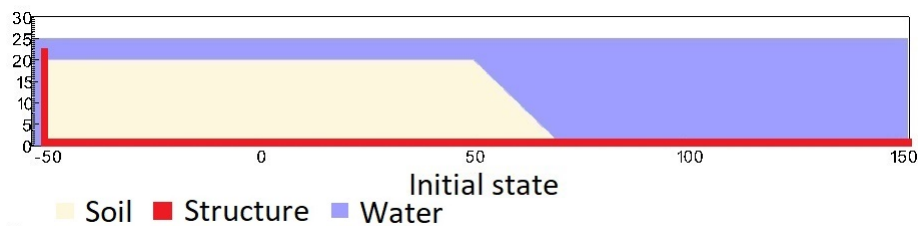


Figure 18: Numerical model simulation of the earthquake-induced submarine landslide

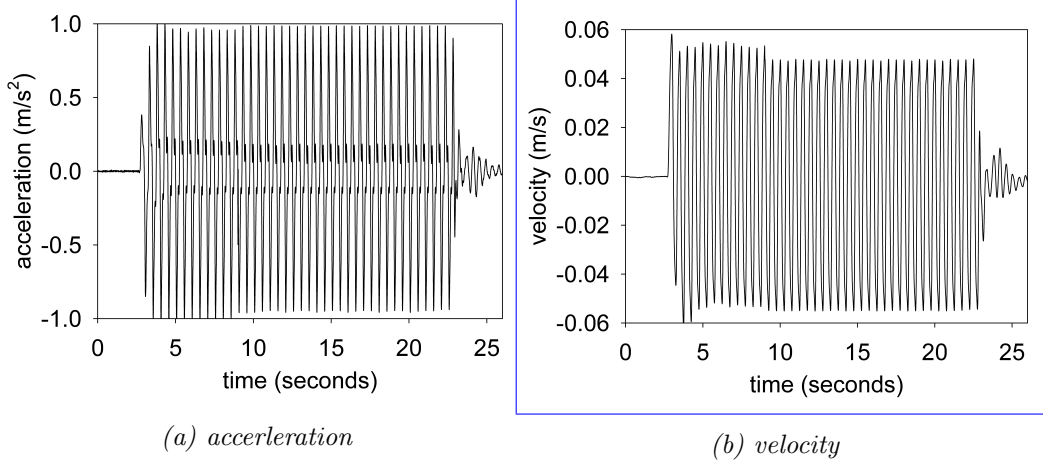


Figure 19: Ground acceleration profile, frequency of 2Hz and magnitude of 1g

In the final example, we perform numerical analysis of the earthquake induced submarine landslides. A plane strain model with the slope under water is shown in Figure 18. A 20m high slope with slope gradient of 45 degrees is placed in a horizontal and vertical structure which was used to be a shaking table to apply earthquake loading. We simplify the earthquake loading by simulating the ground shaking for 20 seconds with the peak constant ground acceleration of 1g and the a constant frequency of 2Hz (Figure 19a). The ground motion is applied in terms of velocity (Figure 19b). The An earthquake of this magnitude can occurred typically for the earthquake of magnitude of more than 6. is possible. For instance, in the case of the 2023 Turkey-Syria Earthquake, significant ground shaking with peak ground acceleration exceeding 1g was observed at numerous locations. This serves as an example of the practical occurrence of such high levels of ground acceleration during seismic events. To generate the seismic loading, the same method was used as presented in the previous numerical example.

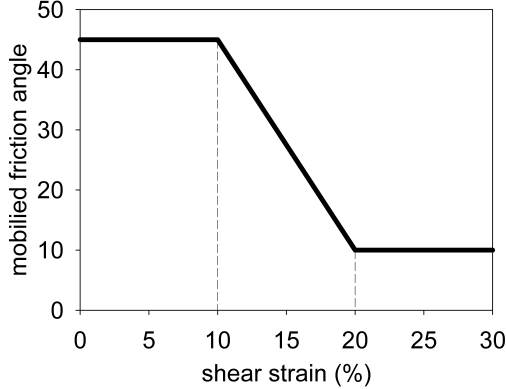


Figure 20: Mobilized friction angle in Mohr Coulomb model

637 A non-associated Mohr-Coulomb model is used for the soil. The soil grain
 638 has the density of 2650 kg/m^3 , Young's modulus of 10 kPa and Poisson's
 639 ratio of 0.3 and zero cohesion. The mobilized friction angle ϕ'_m is governed
 640 following the softening curve (see Figure 20) with the peak friction angle ϕ'_p
 641 of 45 degrees and the residual friction angle ϕ'_r of 10 degrees. The porosity
 642 is 0.3 and the average grain size of the soil is around $0.1 \mu\text{m}$ to mimic the
 643 undrained behavior. The mobilized dilatancy angle is calculated from the
 644 ~~Rowe-stress dilatancy~~ [Rowe's stress dilatancy theory \[28\]](#) as follow:

$$\sin \psi'_m = \frac{\sin \phi'_m - \sin \phi'_r}{1 - (\sin \phi'_r \sin \phi'_m)} \quad (100)$$

645 The solid plane is modeled as a rigid body acted as a shaking table. The con-
 646 tact between horizontal plane and the sand is the frictional contact with the
 647 friction coefficient of 0.1. No artificial damping is applied in the simulation.
 648 The contact between vertical plane and the sand is ~~eonsdered~~ [considered](#) to
 649 be smooth with zero friction coefficient. ~~Under gravity, the density of the~~
 650 ~~water at the surface is 999.8 kg/m^3 at the pressure of 1 atm. At the top~~
 651 ~~boundary, the air has a density of 1.17 kg/m^3 at the atmospheric pressure~~
 652 ~~of 1 atm. At 5 Celcius degrees, air and water have viscosity of $18.45 \text{e}^{-3} \text{ mPa}$~~
 653 ~~s and 1 mPa s respectively.~~ On all boundary faces, the symmetric bound-
 654 ary condition is imposed, while the ~~Neuman~~ [Neumann](#) boundary condition
 655 is imposed at the top ~~boundaryfor~~ [boundary for](#) pressure ($d\rho/dx = 0 \text{ kPa}$)
 656 and density ($d\rho/dx = 0 \text{ kg/m}^3$). [Symmetric boundary condition refers to](#)
 657 [a condition where the normal component of the velocity at the boundary](#)

658 face is set to zero, and the tangential component is equal to the tangential
 659 component of the neighboring cells. The mesh size is 0.25×0.25 m with 300852
 660 element cells and 142316 material points. The simulation takes a couple of
 661 hours to perform 60 seconds of the simulation using 4096 CPUs.

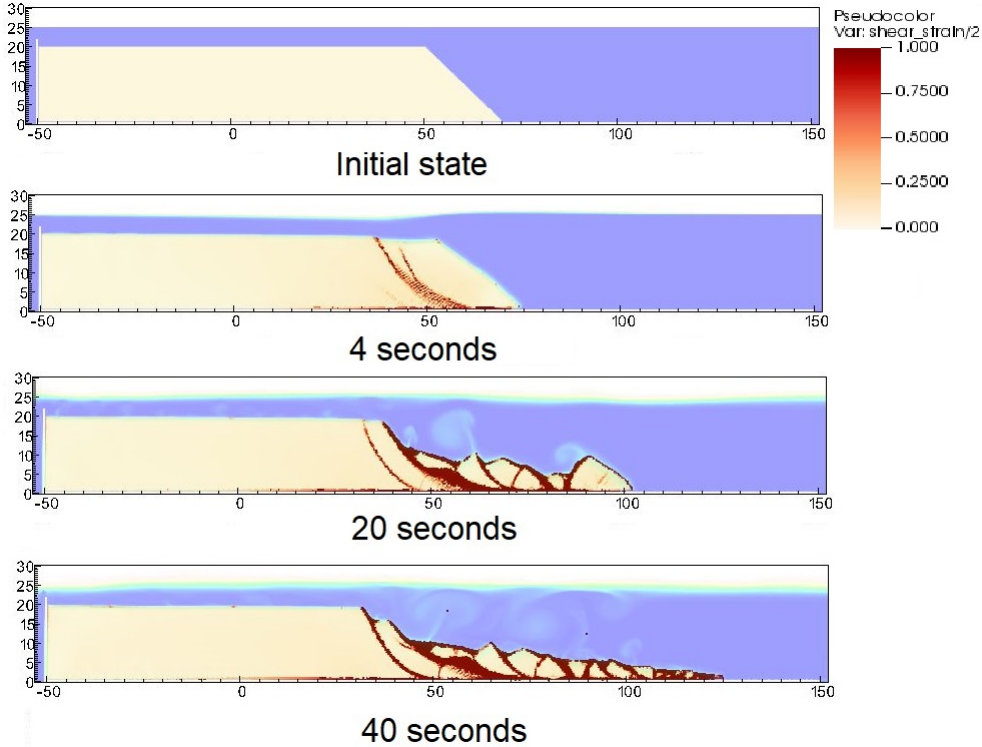


Figure 21: Shear strain during the earthquake-induced submarine landslides

662 We demonstrate the entire process and the mechanism of the earthquake-
 663 induced submarine landslides by showing the shear strain (Figure 21), the
 664 pore water pressure in atm (Figure 22) and the velocity (Figure 23).
 665 The failure mechanism can be characterized as the progressive
 666 failure mechanism. Here are some numerical observation:

- 667 1. At the initial of the seismic event, the seismic loading triggers the
 668 first slide at 3 seconds. At 4 seconds, the debris start to move with the
 669 maximum speed of around 2-3 m/s with multiple shear band developed
 670 in the slope. The wave generated from the submarine slide is around
 671 2-3m towards the slide direction.

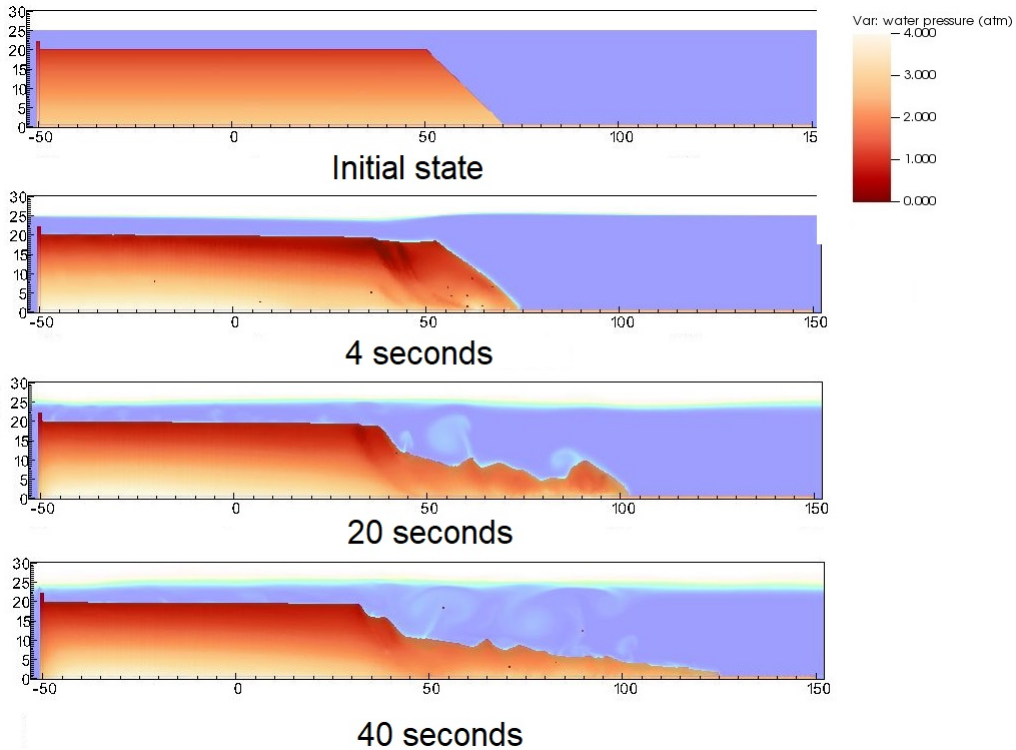


Figure 22: pore water pressure during the earthquake-induced submarine landslides

- 672 2. When the onset of the shear band occurs in the slope (for example
 673 at 4 seconds and 20 seconds), the negative excess pore water pressure
 674 is developed along this shear band with pore water pressure is under
 675 1atm. This is a typical dilatancy behavior when the soil is sheared
 676 rapidly in the undrained behavior.
- 677 3. When the seismic loading ends at 23 seconds, the last shear band is
 678 mobilized and the slope soon reaches to the final deposition. No more
 679 progressive failure developed in the slope. The turbulent flow developed
 680 as the interaction between debris flow and seawater.
- 681 Overall, we show the completed process of the earthquake-induced submarine
 682 landslides involving (1) earthquake triggering mechanism, (2) the onset of the
 683 shear band with the development development of negative excess pore water
 684 pressure, (3) progressive failure mechanism, (4) submarine landslide induced
 685 wave to final deposition.

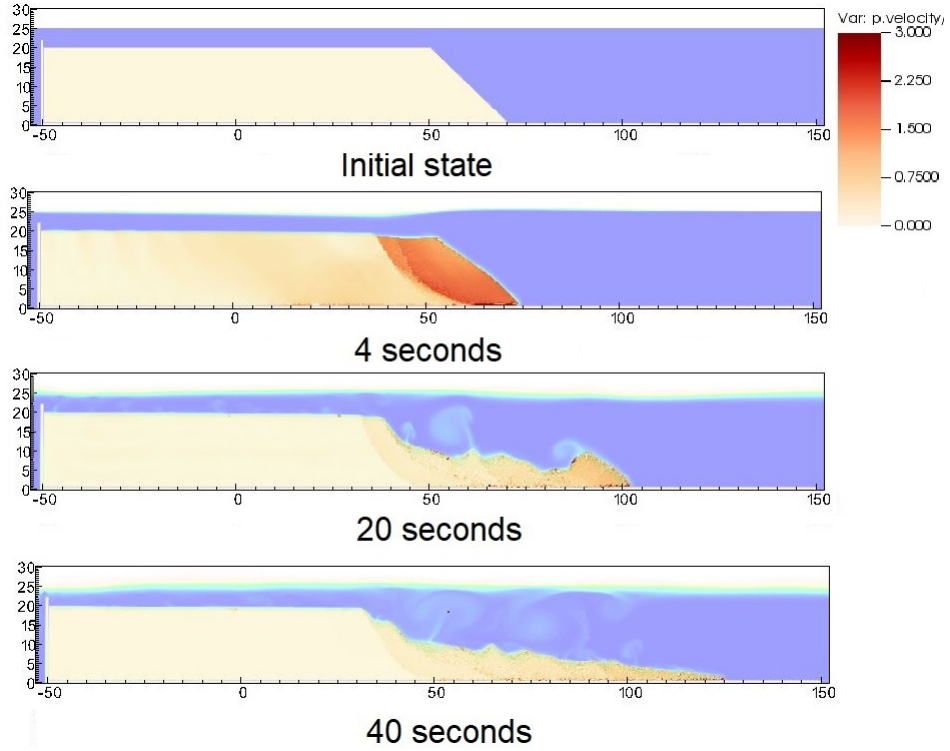


Figure 23: Velocity during the earthquake-induced submarine landslides

686 **Conclusions**

687 We have presented a numerical approach MPMICE for the simulation
 688 of large deformation soil-fluid-structure interaction, emphasizing the simu-
 689 lation of the earthquake-induced submarine landslides. The model uses (1)
 690 the Material Point Method for capturing the large deformation of iso-thermal
 691 porous media and solid structures and (2) Implicit Continuous Eulerian (com-
 692 pressible, conservative multi-material CFD formulation) for modeling the
 693 complex fluid flow including turbulence. This model is implemented in the
 694 high-performance Uintah computational framework and validated against an-
 695 alytical solution and experiment. We then demonstrate the capability of the
 696 model to simulate the entire process of the earthquake induced submarine
 697 landslides.

698 **Acknowledgements**

699 The authors gratefully acknowledge Dr. James Guilkey and Dr. Todd
 700 Harman from the University of Utah for sharing the insight on the theoretical
 701 framework of MPMICE which this work is based. This project has received
 702 funding from the European Union's Horizon 2020 research and innovation
 703 program under the Marie Skłodowska-Curie Actions (MSCA) Individual Fel-
 704 lowship (Project SUBSLIDE "Submarine landslides and their impacts on
 705 offshore infrastructures") grant agreement 101022007. The authors would
 706 also like to acknowledge the support from the Research Council of Norway
 707 through its Centers of Excellence funding scheme, project number 262644
 708 Porelab. The computations were performed on High Performance Comput-
 709 ing resources provided by UNINETT Sigma2 - the National Infrastructure
 710 for High Performance Computing and Data Storage in Norway.

711 **Appendix: Equation derivation**

712 Before deriving the governing equation, we define the Lagrangian deriva-
 713 tive for a state variable f as:

$$\frac{D_f f}{Dt} = \frac{\partial f}{\partial t} + \mathbf{U}_f \cdot \nabla f \quad \frac{D_s f}{Dt} = \frac{\partial f}{\partial t} + \mathbf{U}_s \cdot \nabla f \quad (101)$$

we use some definition following [16] as below:

$$-\frac{1}{V} \left[\frac{\partial V_f}{\partial p} \right] \equiv \kappa_f \quad \text{isothermal compressibility of fluid} \quad (102)$$

$$\frac{1}{V} \left[\frac{\partial V_f}{\partial T} \right] \equiv \alpha_f \quad \text{constant pressure thermal expansivity of fluid} \quad (103)$$

714 Then, the rate of volume with incompressible solid grains are calculated as
 715 belowbelow:

$$\frac{1}{V} \frac{D_f V_f}{Dt} = \frac{1}{V} \left(\left[\frac{\partial V_f}{\partial p} \right] \frac{D_f P_{eq}}{Dt} + \left[\frac{\partial V_f}{\partial T_f} \right] \frac{D_f T_f}{Dt} \right) = \frac{1}{V} \left(-\kappa_f \frac{D_f P_{eq}}{Dt} + \alpha_f \frac{D_f T_f}{Dt} \right) \quad (104)$$

716 *Evolution of porosity*

717 Solving the solid mass balance equation (4) with the definition of solid
 718 mass in equation (2), it leads to the rate of porosity as belowbelows:

$$\frac{D_s m_s}{Dt} = \frac{D_s(\phi_s \rho_s V)}{Dt} = \rho_s V \frac{D_s \phi_s}{Dt} + \phi_s V \frac{D_s \rho_s}{Dt} + \phi_s \rho_s \frac{D_s V}{Dt} = 0 \quad (105)$$

719 The soil grains are assumed to be incompressible, therefore, term 2 in the
 720 right hand side is zero. leading to:

$$V \frac{D_s \phi_s}{Dt} + \phi_s \frac{D_s V}{Dt} = 0 \quad (106)$$

721 Dividing all terms with V with the equation $\frac{1}{V} \frac{D_s V}{Dt} = \nabla \cdot \mathbf{U}_s$, it leads to:

$$\frac{D_s n}{Dt} = \frac{\partial n}{\partial t} + \mathbf{U}_s \cdot \nabla n = \phi_s \nabla \cdot \mathbf{U}_s \quad (107)$$

722 *Momentum conservation*

723 The linear momentum balance equationequations for the fluid phases
 724 based on mixture theory isare:

$$\frac{1}{V} \frac{D_f(m_f \mathbf{U}_f)}{Dt} = \nabla \cdot (-\phi_f p_f \mathbf{I}) + \nabla \cdot \boldsymbol{\tau}_f + \bar{\rho}_f \mathbf{b} + \sum \mathbf{f}_d + \mathbf{f}_b \quad (108)$$

726 On the right hand sand, the first term is the divergence of partial fluid phase
 727 stress, the third term is the body force, the fourth term is the drag force
 728 (momentum exchange) and the fifth term is the buoyant force described in
 729 [29] for the immiscible mixtures. The buoyant force is in the form asbelows:

$$\mathbf{f}_b = \boldsymbol{\sigma}_f \nabla(n) \quad (109)$$

731 As a result, the linear momentum balance equationequations for the fluid
 732 phases beeomesbecome as:

$$\frac{1}{V} \frac{D_f(m_f \mathbf{U}_f)}{Dt} = \frac{1}{V} \left[\frac{\partial(m_f \mathbf{U}_f)}{\partial t} + \nabla \cdot (m_f \mathbf{U}_f \mathbf{U}_f) \right] = -\phi_f \nabla p_f + \nabla \cdot \boldsymbol{\tau}_f + \bar{\rho}_f \mathbf{b} + \sum \mathbf{f}_d \quad (110)$$

733 The Reynolds stress component can be included in the term $\boldsymbol{\tau}_f$ to consider the
 734 turbulent effects if needed. To derive the linear momentum balance equation

735 for the solid phase, we begin with the linear momentum balance equation for
 736 the mixture as:

$$\frac{1}{V} \frac{D_f(m_f \mathbf{U}_f)}{Dt} + \frac{1}{V} \frac{D_s(m_s \mathbf{U}_s)}{Dt} = \nabla \cdot (\boldsymbol{\sigma}) + \bar{\rho}_f \mathbf{b} + \bar{\rho}_s \mathbf{b} \quad (111)$$

737 Combining Terzaghi's equation (3) and subtracting both sides with equation
 738 (110), we obtain the linear momentum balance ~~equation~~equations for the
 739 solid phase as:

$$\frac{1}{V} \frac{D_s(m_s \mathbf{U}_s)}{Dt} = \nabla \cdot (\boldsymbol{\sigma}') - \phi_s \nabla p_f + \bar{\rho}_s \mathbf{b} - \sum \mathbf{f}_d + \sum \mathbf{f}_{fric} \quad (112)$$

740 Here the \mathbf{f}_{fric} stems from the soil-structure interaction following the contact
 741 law between the soil/structure ~~interaces~~interfaces.

742 Energy conservation

743 We adopt the general form of the total energy balance equation for the
 744 porous media from [30], the total energy balance equations for the fluid phases
 745 are:

$$\frac{1}{V} \frac{D_f(m_f(e_f + 0.5 \mathbf{U}_f^2))}{Dt} = \nabla \cdot (-np_f \mathbf{I}) \cdot \mathbf{U}_f + \nabla \cdot \mathbf{q}_f + (\bar{\rho}_f \mathbf{b}) \cdot \mathbf{U}_f + \sum \mathbf{f}_d \cdot \mathbf{U}_f + \sum q_{sf} \quad (113)$$

746 Applying the product rule $D(m\mathbf{U}^2) = D(m\mathbf{U} \cdot \mathbf{U}) = 2\mathbf{U} \cdot D(m\mathbf{U})$, the left
 747 hand side of equation (113) becomes:

$$\frac{1}{V} \frac{D_f(m_f(e_f + 0.5 \mathbf{U}_f^2))}{Dt} = \frac{1}{V} \frac{D_f(m_f e_f)}{Dt} + \frac{1}{V} \frac{D_f(m_f \mathbf{U}_f)}{Dt} \cdot \mathbf{U}_f \quad (114)$$

748 Combining equations (110), (113), (114), we obtain the final form of the
 749 internal energy balance equation for the fluid phases as:

$$\frac{1}{V} \frac{D_f(m_f e_f)}{Dt} = \frac{1}{V} \left[\frac{\partial(m_f e_f)}{\partial t} + \nabla \cdot (m_f e_f \mathbf{U}_f) \right] = \bar{\rho}_f p_f \frac{D_f v_f}{Dt} + \nabla \cdot \mathbf{q}_f + \sum q_{sf} \quad (115)$$

750 On the right hand side, the terms include the average pressure-volume work,
 751 the average viscous dissipation, the thermal transport and the energy ex-
 752 change between solid and fluid respectively. The heat flux is $\mathbf{q}_f = \bar{\rho}_f \beta_f \nabla T_f$
 753 with β_f being the thermal conductivity coefficient. To derive the internal
 754 energy balance equation for the solid phase, we introduce the rate of the
 755

756 internal energy for the thermoelastic materials as a function of elastic strain
 757 tensor $\boldsymbol{\epsilon}_s^e$ and temperature T_s as belows:

$$\frac{m_s}{V} \frac{D_s(e_s)}{Dt} = \boldsymbol{\sigma}' : \frac{D_s(\boldsymbol{\epsilon}_s^e)}{Dt} + \frac{D_s(e_s)}{D_s(T_s)} \frac{D_s(T_s)}{Dt} = \boldsymbol{\sigma}' : \frac{D_s(\boldsymbol{\epsilon}_s^e)}{Dt} + c_v \frac{D_s(T_s)}{Dt} \quad (116)$$

758 c_v is the specific heat at the constant volume of the solid materials. The total
 759 energy balance equation for the mixture based on [30] can be written as:

$$\begin{aligned} \frac{1}{V} \frac{D_f(m_f(e_f + 0.5\mathbf{U}_f^2))}{Dt} + \frac{1}{V} \frac{D_s(m_s(e_s + 0.5\mathbf{U}_s^2))}{Dt} &= \nabla \cdot (-\phi_f p_f \mathbf{I}) \cdot \mathbf{U}_f \\ &+ \nabla \cdot (\boldsymbol{\sigma}' - \phi_s p_f \mathbf{I}) \cdot \mathbf{U}_s + (-\phi_f p_f \mathbf{I}) : \nabla \mathbf{U}_f + \boldsymbol{\sigma}' : \nabla \mathbf{U}_s \\ &+ (\bar{\rho}_f \mathbf{b}) \cdot \mathbf{U}_f + (\bar{\rho}_s \mathbf{b}) \cdot \mathbf{U}_s + \nabla \cdot \mathbf{q}_f + \nabla \cdot \mathbf{q}_s + \sum \mathbf{f}_d \cdot (\mathbf{U}_f - \mathbf{U}_s) \end{aligned} \quad (117)$$

761 Subtracting equation (117), (116) to equations (113) and (112), we obtained
 762 the internal energy balance equation for solid phase as:

$$\boldsymbol{\sigma}' : \frac{D_s(\boldsymbol{\epsilon}_s^e)}{Dt} + \frac{m_s}{V} c_v \frac{D_s(T_s)}{Dt} = \Delta W_s + \Delta W_{friction} + \nabla \cdot \mathbf{q}_s - \sum q_{sf} \quad (118)$$

763 On the right hand side, the terms include the work rate from frictional sliding
 764 between solid materials $\Delta W_{friction}$, thermal transport and energy exchange
 765 between solid and fluid respectively. The heat flux is $\mathbf{q}_s = \bar{\rho}_s \beta_s \nabla T_s$ with β_s
 766 being the thermal conductivity of the solid materials, the mechanical work
 767 rate $\Delta W_s = \boldsymbol{\sigma}' : \frac{D_s(\boldsymbol{\epsilon}_s^e)}{Dt} = \boldsymbol{\sigma}' : (\frac{D_s(\boldsymbol{\epsilon}_s^e)}{Dt} + \frac{D_s(\boldsymbol{\epsilon}_s^p)}{Dt})$ computed from the constitutive
 768 model with $\boldsymbol{\epsilon}_s^p$ is the plastic strain tensor, . By subtracting the term $\boldsymbol{\sigma}' : \frac{D_s(\boldsymbol{\epsilon}_s^e)}{Dt}$,
 769 we get the final form of the energy balance equation as:

$$\frac{m_s}{V} c_v \frac{D_s(T_s)}{Dt} = \boldsymbol{\sigma}' : \frac{D_s(\boldsymbol{\epsilon}_s^p)}{Dt} + \Delta W_{friction} + \nabla \cdot \mathbf{q}_s - \sum q_{sf} \quad (119)$$

770 Advanced Fluid Pressure

771 The discretization of the pressure equation begins with the Lagrangian
 772 face-centered cell face velocity and the equation for the pressure as:

$$\bar{\rho}_{f,FC} \frac{\mathbf{U}_{f,FC}^{n+1} - \mathbf{U}_{f,FC}^n}{dt} = n \nabla^{FC} P_{\textcolor{red}{fc}\textcolor{blue}{f,c}}^{n+1} + \bar{\rho}_{f,FC} \mathbf{b} \quad (120)$$

$$773 \quad \kappa \frac{dP}{dt} = \nabla^c \cdot \mathbf{U}_{f,FC}^{n+1} \quad (121)$$

774 The divergence of the equation (120) with $\nabla \cdot \mathbf{b} = 0$ is:

$$\nabla^c \cdot \mathbf{U}_{f,FC}^{n+1} - \nabla^c \cdot \mathbf{U}_{f,FC}^n = \nabla^c \frac{\Delta t}{\rho_{f,FC}^n} \cdot \nabla^{FC} (P_{fc,fc}^n + \Delta P_{fc,fc}^n) \quad (122)$$

775 To solve this equation, we define the ~~face-centered-cell face~~ intermediate
776 velocity $\mathbf{U}_{f,FC}^*$ as:

$$\bar{\rho}_{f,FC} \frac{\mathbf{U}_{f,FC}^* - \mathbf{U}_{f,FC}^n}{\Delta t} = n \nabla^{FC} P_{fc,fc}^n + \bar{\rho}_{f,FC} \mathbf{b} \quad (123)$$

777 The divergence of the equation (123) is:

$$\nabla^c \cdot \mathbf{U}_{f,FC}^* - \nabla^c \cdot \mathbf{U}_{f,FC}^n = \nabla^c \frac{\Delta t}{\rho_{f,FC}^n} \cdot \nabla^{FC} P_{fc,fc}^n \quad (124)$$

778 Combining equations (121, 122, 124), it leads to:

$$\left(\kappa - \nabla^c \frac{\Delta t}{\rho_{f,FC}^n} \cdot \nabla^{FC} \right) \Delta P_{fc}^n = -\nabla^c \cdot \mathbf{U}_{f,FC}^* \quad (125)$$

779 When the fluid is incompressible, κ approaches to zero and the equation
780 (125) becomes the Poisson's equation for the incompressible fluid flow.

781 *Momentum and Energy exchange with an implicit solver*

782 Considering the fluid momentum balance equation as:

$$(m\mathbf{U})_{f,FC}^{n+1} = (m\mathbf{U})_{f,FC}^n - \Delta t (Vn \nabla^{FC} P_{fc,fc}^n + m_f \mathbf{b}) + VK \Delta t (\mathbf{U}_{s,FC}^{n+1} - \mathbf{U}_{f,FC}^{n+1}) \quad (126)$$

783 Assuming And assuming $m_{f,FC}^{n+1} = m_{f,FC}^n$ we get, we get:

$$\mathbf{U}_{f,FC}^{n+1} = \mathbf{U}_{f,FC}^n - \Delta t \left(\frac{\nabla^{FC} P_{fc}^n}{\rho_{f,FC}^n} + \mathbf{b} \right) + \frac{\Delta t K}{\rho_{f,FC}^n} (\mathbf{U}_{s,FC}^{n+1} - \mathbf{U}_{f,FC}^{n+1}) \quad (127)$$

784 As defined in the section 'Advanced Fluid Pressure', the ~~face-centered-cell~~
785 ~~face~~ intermediate fluid velocity $\mathbf{U}_{f,FC}^* = \Delta t (\nabla^{FC} P_{fc}^n / \rho_{f,FC}^n + \mathbf{b})$ leading to is
786 computed as:

$$\mathbf{U}_{f,FC}^{n+1} = \mathbf{U}_{f,FC}^* + \frac{\Delta t K}{\rho_{f,FC}^n} (\mathbf{U}_{s,FC}^{n+1} - \mathbf{U}_{f,FC}^{n+1}) \quad (128)$$

787 Considering the solid momentum balance equation as:

$$(m\mathbf{U})_{s,FC}^{n+1} = (m\mathbf{U})_{s,FC}^n - \Delta t(V\nabla^{FC} \cdot \boldsymbol{\sigma}'^n - V(1-n)\nabla^{FC}P_{fc,fc}^n + m_s\mathbf{b}) - VK\Delta t(\mathbf{U}_{s,FC}^{n+1} - \mathbf{U}_{f,FC}^{n+1}) \quad (129)$$

788 We define the face-centered cell face intermediate solid velocity as $\mathbf{U}_{s,FC}^* = \Delta t(\nabla^{FC} \cdot \boldsymbol{\sigma}_c'^n / \bar{\rho}_{s,FC} - \nabla^{FC}P_{f,fc}^n / \rho_s + \mathbf{b})$
 789 leading to $\mathbf{U}_{s,FC}^* = \Delta t(\nabla^{FC} \cdot \boldsymbol{\sigma}_c'^n / \bar{\rho}_{s,FC} - \nabla^{FC}P_{f,fc}^n / \rho_s + \mathbf{b})$ leading to:

$$\mathbf{U}_{s,FC}^{n+1} = \mathbf{U}_{s,FC}^* - \frac{\Delta t K}{\bar{\rho}_{s,FC}^n} (\mathbf{U}_{s,FC}^{n+1} - \mathbf{U}_{f,FC}^{n+1}) \quad (130)$$

790 Combining equation (128) and (130) we get:

$$\begin{aligned} \mathbf{U}_{f,FC}^* + \Delta\mathbf{U}_{f,FC} &= \mathbf{U}_{f,FC}^* + \frac{\Delta t K}{\bar{\rho}_{f,FC}^n} (\mathbf{U}_{s,FC}^* + \Delta\mathbf{U}_{s,FC} - \mathbf{U}_{f,FC}^* - \Delta\mathbf{U}_{f,FC}) \\ \mathbf{U}_{s,FC}^* + \Delta\mathbf{U}_{s,FC} &= \mathbf{U}_{s,FC}^* - \frac{\Delta t K}{\bar{\rho}_{s,FC}^n} (\mathbf{U}_{s,FC}^* + \Delta\mathbf{U}_{s,FC} - \mathbf{U}_{f,FC}^* - \Delta\mathbf{U}_{f,FC}) \end{aligned} \quad (131)$$

791 Rearranging the equation (131), it leads to the linear system of equations as
 792 belows:

$$\begin{vmatrix} (1 + \beta_{12,FC}) & -\beta_{12,FC} \\ -\beta_{21,FC} & (1 + \beta_{21,FC}) \end{vmatrix} \begin{vmatrix} \Delta\mathbf{U}_{f,FC} \\ \Delta\mathbf{U}_{s,FC} \end{vmatrix} = \begin{vmatrix} \beta_{12,FC}(\mathbf{U}_{s,FC}^* - \mathbf{U}_{f,FC}^*) \\ \beta_{21,FC}(\mathbf{U}_{f,FC}^* - \mathbf{U}_{s,FC}^*) \end{vmatrix}$$

793 Solving this linear equations with $\beta_{12,FC} = (\Delta t K) / \bar{\rho}_{f,FC}^n$ and $\beta_{21,FC} = (\Delta t K) / \bar{\rho}_{s,FC}^n$ with K is the momentum exchange coefficient. Similar derivation can be performed to computed the cell-center velocity increment leading to:

$$\begin{vmatrix} (1 + \beta_{12c}) & -\beta_{12c} \\ -\beta_{21c} & (1 + \beta_{21c}) \end{vmatrix} \begin{vmatrix} \Delta\mathbf{U}_{fc,fc} \\ \Delta\mathbf{U}_{sc} \end{vmatrix} = \begin{vmatrix} \beta_{12c}(\mathbf{U}_{sc}^* - \mathbf{U}_{fc,fc}^*) \\ \beta_{21c}(\mathbf{U}_{fc,fc}^* - \mathbf{U}_{sc}^*) \end{vmatrix}$$

797 with $\beta_{12c} = (\Delta t K) / \bar{\rho}_{fc}^n$, $\beta_{12c} = (\Delta t K) / \bar{\rho}_{fc}^n$ and $\beta_{21c} = (\Delta t K) / \bar{\rho}_{sc}^n$ and the
 798 cell-centered intermediate velocity can be calculated by:

$$\begin{aligned} \mathbf{U}_{fc,fc}^* &= \mathbf{U}_{fc,fc}^n + \Delta t \left(-\frac{\nabla P_{fc}^{n+1}}{\bar{\rho}_{fc}^n} \frac{\nabla P_{f,fc}^{n+1}}{\bar{\rho}_{f,fc}^n} + \frac{\nabla \cdot \boldsymbol{\tau}_{fc}^n}{\bar{\rho}_{fc}^n} \frac{\nabla \cdot \boldsymbol{\tau}_{f,fc}^n}{\bar{\rho}_{f,fc}^n} + \mathbf{b} \right) \\ \mathbf{U}_{sc}^* &= \mathbf{U}_{sc}^n + \Delta t \left(\frac{\nabla \cdot \boldsymbol{\sigma}_c'^n}{\bar{\rho}_{sc}^n} - \frac{\nabla P_{fc}^{n+1}}{\bar{\rho}_s} \frac{\nabla P_{f,fc}^{n+1}}{\bar{\rho}_s} + \mathbf{b} \right) \end{aligned} \quad (132)$$

799 For generalize multi materials i,j = 1:N, the linear equations is in the form
800 as:

$$\begin{vmatrix} (1 + \beta_{ij}) & -\beta_{ij} \\ -\beta_{ji} & (1 + \beta_{ji}) \end{vmatrix} \begin{vmatrix} \Delta \mathbf{U}_i \\ \Delta \mathbf{U}_j \end{vmatrix} = \begin{vmatrix} \beta_{ij}(\mathbf{U}_i^* - \mathbf{U}_j^*) \\ \beta_{ji}(\mathbf{U}_j^* - \mathbf{U}_i^*) \end{vmatrix}$$

801 Similar approach applied for the ernergy exchange term leading to:

$$\begin{vmatrix} (1 + \eta_{ij}) & -\eta_{ij} \\ -\eta_{ji} & (1 + \eta_{ji}) \end{vmatrix} \begin{vmatrix} \Delta T_i \\ \Delta T_j \end{vmatrix} = \begin{vmatrix} \eta_{ij}(T_i^n - T_j^n) \\ \eta_{ji}(T_j^n - T_i^n) \end{vmatrix}$$

802 with η is the energy exchange coefficient.

803 References

- 804 [1] D. Yuk, S. Yim, P.-F. Liu, Numerical modeling of submarine mass-
805 movement generated waves using RANS model, Computers and Geo-
806 sciences 32 (7) (2006) 927–935. doi:10.1016/j.cageo.2005.10.028.
807 URL <https://doi.org/10.1016/j.cageo.2005.10.028>
- 808 [2] S. Glimsdal, J.-S. L'Heureux, C. B. Harbitz, F. Løvholt, The 29th jan-
809 uary 2014 submarine landslide at statland, norway—landslide dynamics,
810 tsunami generation, and run-up, Landslides 13 (6) (2016) 1435–1444.
811 doi:10.1007/s10346-016-0758-7.
812 URL <https://doi.org/10.1007/s10346-016-0758-7>
- 813 [3] S. Abadie, D. Morichon, S. Grilli, S. Glockner, Numerical sim-
814 ulation of waves generated by landslides using a multiple-fluid
815 navier–stokes model, Coastal Engineering 57 (9) (2010) 779–794.
816 doi:10.1016/j.coastaleng.2010.03.003.
817 URL <https://doi.org/10.1016/j.coastaleng.2010.03.003>
- 818 [4] M. Rauter, S. Viroulet, S. S. Gylfadóttir, W. Fellin, F. Løvholt, Granular
819 porous landslide tsunami modelling – the 2014 lake askja flank collapse,
820 Nature Communications 13 (1) (Feb. 2022). doi:10.1038/s41467-022-
821 28296-7.
822 URL <https://doi.org/10.1038/s41467-022-28296-7>
- 823 [5] Q.-A. Tran, W. Sołowski, Generalized interpolation material point
824 method modelling of large deformation problems including strain-
825 rate effects – application to penetration and progressive fail-
826 ure problems, Computers and Geotechnics 106 (2019) 249–265.

- 827 doi:10.1016/j.compgeo.2018.10.020.
828 URL <https://doi.org/10.1016/j.compgeo.2018.10.020>
- 829 [6] T. Capone, A. Panizzo, J. J. Monaghan, SPH modelling of water
830 waves generated by submarine landslides, *Journal of Hydraulic Research*
831 48 (sup1) (2010) 80–84. doi:10.1080/00221686.2010.9641248.
832 URL <https://doi.org/10.1080/00221686.2010.9641248>
- 833 [7] X. Zhang, E. Oñate, S. A. G. Torres, J. Bleyer, K. Krabbenhoft, A
834 unified lagrangian formulation for solid and fluid dynamics and its possi-
835 bility for modelling submarine landslides and their consequences, *Com-
836 puter Methods in Applied Mechanics and Engineering* 343 (2019) 314–
837 338. doi:10.1016/j.cma.2018.07.043.
838 URL <https://doi.org/10.1016/j.cma.2018.07.043>
- 839 [8] R. Dey, B. C. Hawlader, R. Phillips, K. Soga, Numerical modelling
840 of submarine landslides with sensitive clay layers, *Géotechnique* 66 (6)
841 (2016) 454–468. doi:10.1680/jgeot.15.p.111.
842 URL <https://doi.org/10.1680/jgeot.15.p.111>
- 843 [9] S. Bandara, K. Soga, Coupling of soil deformation and pore fluid flow
844 using material point method, *Computers and Geotechnics* 63 (2015)
845 199–214. doi:10.1016/j.compgeo.2014.09.009.
846 URL <https://doi.org/10.1016/j.compgeo.2014.09.009>
- 847 [10] A. P. Tampubolon, T. Gast, G. Klár, C. Fu, J. Teran, C. Jiang,
848 K. Museth, Multi-species simulation of porous sand and water
849 mixtures, *ACM Transactions on Graphics* 36 (4) (2017) 1–11.
850 doi:10.1145/3072959.3073651.
851 URL <https://doi.org/10.1145/3072959.3073651>
- 852 [11] A. S. Baumgarten, K. Kamrin, A general constitutive model for dense,
853 fine-particle suspensions validated in many geometries, *Proceedings
854 of the National Academy of Sciences* 116 (42) (2019) 20828–20836.
855 doi:10.1073/pnas.1908065116.
856 URL <https://doi.org/10.1073/pnas.1908065116>
- 857 [12] Q.-A. Tran, W. Sołowski, Temporal and null-space filter for the ma-
858 terial point method, *International Journal for Numerical Methods in*

- 859 Engineering 120 (3) (2019) 328–360. doi:10.1002/nme.6138.
860 URL <https://doi.org/10.1002/nme.6138>
- 861 [13] X. Zheng, F. Pisanò, P. J. Vardon, M. A. Hicks, An explicit stabilised
862 material point method for coupled hydromechanical problems in two-
863 phase porous media, Computers and Geotechnics 135 (2021) 104112.
864 doi:10.1016/j.compgeo.2021.104112.
865 URL <https://doi.org/10.1016/j.compgeo.2021.104112>
- 866 [14] Q. A. Tran, W. Sołowski, M. Berzins, J. Guilkey, A convected particle
867 least square interpolation material point method, International Journal
868 for Numerical Methods in Engineering 121 (6) (2019) 1068–1100.
869 doi:10.1002/nme.6257.
870 URL <https://doi.org/10.1002/nme.6257>
- 871 [15] J.-S. Chen, M. Hillman, S.-W. Chi, Meshfree methods: Progress made
872 after 20 years, Journal of Engineering Mechanics 143 (4) (Apr. 2017).
873 doi:10.1061/(asce)em.1943-7889.0001176.
874 URL [https://doi.org/10.1061/\(asce\)em.1943-7889.0001176](https://doi.org/10.1061/(asce)em.1943-7889.0001176)
- 875 [16] B. A. Kashiwa, A multifield model and method for fluid-structure in-
876 teraction dynamics, Tech. Rep. LA-UR-01-1136, Los Alamos National
877 Laboratory (2001).
- 878 [17] J. Guilkey, T. Harman, B. Banerjee, An eulerian–lagrangian
879 approach for simulating explosions of energetic devices,
880 Computers and Structures 85 (11) (2007) 660 – 674.
881 doi:<https://doi.org/10.1016/j.compstruc.2007.01.031>.
882 URL <http://www.sciencedirect.com/science/article/pii/S0045794907000429>
- 883 [18] A. S. Baumgarten, B. L. Couchman, K. Kamrin, A coupled finite volume
884 and material point method for two-phase simulation of liquid–sediment
885 and gas–sediment flows, Computer Methods in Applied Mechanics and
886 Engineering 384 (2021) 113940. doi:10.1016/j.cma.2021.113940.
887 URL <https://doi.org/10.1016/j.cma.2021.113940>
- 888 [19] S. Bardenhagen, J. Guilkey, K. Roessig, J. Brackbill, W. Witzel,
889 J.C.Foster, An improved contact algorithm for the material point
890 method and application to stress propagation in granular material,

- 891 CMES-Computer Modeling in Engineering and Sciences 2 (2001) 509–
892 522. doi:10.3970/cmes.2001.002.509.
- 893 [20] J. A. M. K. R. Beetstra, M. A. van der Hoef, Drag force of intermediate
894 reynolds number flow past mono- and bidisperse arrays of spheres,
895 Fluid Mechanics and Transport Phenomena 53 (2) (2007) 489 – 501.
896 doi:<https://doi.org/10.1002/aic.11065>.
- 897 [21] R. W. Stewart, The air-sea momentum exchange, Boundary-Layer Me-
898 teorology 6 (1-2) (1974) 151–167. doi:10.1007/bf00232481.
899 URL <https://doi.org/10.1007/bf00232481>
- 900 [22] S. G. Bardenhagen, E. M. Kober, The generalized interpolation material
901 point method, Computer Modeling in Engineering and Sciences 5 (2004)
902 477–496. doi:10.1016/j.compgeo.2021.104199.
903 URL <https://doi.org/10.3970/cmes.2004.005.477>
- 904 [23] S. G. Amiri, E. Taheri, A. Lavasan, A hybrid finite element model for
905 non-isothermal two-phase flow in deformable porous media, Computers
906 and Geotechnics 135 (2021) 104199. doi:10.1016/j.compgeo.2021.104199.
907 URL <https://doi.org/10.1016/j.compgeo.2021.104199>
- 908 [24] S. A. R. C. Mariotti;, P. Heinrich, Numerical simulation of sub-
909 marine landslides and their hydraulic effects, Journal of Wa-
910 terway, Port, Coastal, and Ocean Engineering 123 (4) (1997).
911 doi:[https://doi.org/10.1061/\(ASCE\)0733-950X\(1997\)123:4\(149\).](https://doi.org/10.1061/(ASCE)0733-950X(1997)123:4(149).)
- 912 [25] A. Alsardi, A. Yerro, Runout Modeling of Earthquake-Triggered
913 Landslides with the Material Point Method, pp. 21–31.
914 arXiv:<https://ascelibrary.org/doi/pdf/10.1061/9780784483428.003>,
915 doi:10.1061/9780784483428.003.
916 URL <https://ascelibrary.org/doi/abs/10.1061/9780784483428.003>
- 917 [26] H. N., O. A., B. H. H., R. P., R. Fukagawa, Seismic slope failuremod-
918 elling using the mesh-free sph method, International Journal of Geomate
919 (2013) 660–665.
- 920 [27] T. Bhandari, F. Hamad, C. Moormann, K. Sharma,
921 B. Westrich, Numerical modelling of seismic slope failure us-
922 ing mpm, Computers and Geotechnics 75 (2016) 126–134.

- 923 doi:<https://doi.org/10.1016/j.compgeo.2016.01.017>.
924 URL <https://www.sciencedirect.com/science/article/pii/S0266352X16000264>
- 925 [28] D. Muir Wood, Soil behaviour and critical state soil mechanics, Cam-
926 bridge University Press, United Kingdom, 1990.
- 927 [29] D. Drumheller, On theories for reacting immiscible mixtures, Inter-
928 national Journal of Engineering Science 38 (3) (2000) 347 – 382.
929 doi:[https://doi.org/10.1016/S0020-7225\(99\)00047-6](https://doi.org/10.1016/S0020-7225(99)00047-6).
930 URL <http://www.sciencedirect.com/science/article/pii/S0020722599000476>
- 931 [30] S. Hassanzadeh, Derivation of basic equations of mass transport in
932 porous media, part1: Macroscopic balance laws, Advances in Wa-
933 ter Resources 9 (1986) 196–206. doi:[https://doi.org/10.1016/0309-1708\(86\)90024-2](https://doi.org/10.1016/0309-1708(86)90024-2).
- 934